MID-AMERICA
TRANSPORTATION CENTER

Report # MATC-MST: 114

Final Report
25-1121-0001-114 (also reporting for 25-1121-0001-242)

Pilot Study on Rugged Fiber Optic Brillouin Sensors for Large-Strain Measurements to Ensure the Safety of Transportation Structures

Genda Chen, Ph.D., P.E., F.ASCE
Professor
Department of Civil, Architectural, and Environmental Engineering
Missouri University of Science and Technology

Zhi Zhou, Ph.D.
Graduate Research Assistant
Hai Xiao, Ph.D.
Professor
Ying Huang, Ph.D. Candidate
Graduate Research Assistant

2012

A Cooperative Research Project sponsored by the
U.S. Department of Transportation Research and
Innovative Technology Administration

Pilot Study on Rugged Fiber Optic Brillouin Sensors for Large-Strain Measurements to Ensure the Safety of Transportation Structures

Genda Chen, Ph.D., P.E., F.ASCE
Professor
Department of Civil, Architectural, and Environmental Engineering
Missouri University of Science and Technology

Zhi Zhou, Ph.D.
Research Associate
Department of Civil, Architectural, and Environmental Engineering
Missouri University of Science and Technology

Hai Xiao, Ph.D.
Professor
Department of Electrical and Computer Engineering
Missouri University of Science and Technology

Ying Huang
Ph.D. Candidate
Department of Civil, Architectural, and Environmental Engineering
Missouri University of Science and Technology

A Report on Research Sponsored by

Mid-America Transportation Center

University of Nebraska–Lincoln

US DOT Research and Innovative Technology Administration

Center for Infrastructure Engineering Studies, Missouri University of Science and Technology

July 2012

Technical Report Documentation Page

1. Report No. 25-1121-0001-114 (25-1121-0001-242 served as a supplemental project within this project)	2. Government Accession No.	3. Recipient's Catalog No.
4. Title and Subtitle Pilot Study on Rugged Fiber Optic Brillouin Sensors for Large-Strain Measurements to Ensure the Safety of Transportation Structures		5. Report Date July 2012
		6. Performing Organization Code
7. Author(s) Genda Chen, Zhi Zhou, Hai Xiao, Ying Huang		8. Performing Organization Report No. 25-1121-0001-114 (25-1121-0001-242 served as a supplemental project within this project)
9. Performing Organization Name and Address Mid-America Transportation Center 2200 Vine St. PO Box 830851 Lincoln, NE 68583-0851		10. Work Unit No. (TRAIS)
		11. Contract or Grant No.
12. Sponsoring Agency Name and Address Research and Innovative Technology Administration 1200 New Jersey Ave., SE Washington, D.C. 20590		13. Type of Report and Period Covered Final Report, April 2008–June 2012
		14. Sponsoring Agency Code MATC TRB RiP No. 17139 (this listing includes the scope of both MATC project numbers associated with this project)
15. Supplementary Notes		

16. Abstract

Brillouin-scattering Optical Time Domain Reflectometry (BOTDR) is a viable technology for simultaneous, distributed strain and temperature measurements for miles-long transportation structures. It is a promising tool to ensure the smooth operation and safety of bridge structures that are key links in surface transportation networks or between various transportation modes: i.e., from airport to train station. Currently, telecom-grade optical fibers are widely used in civil engineering for strain and temperature measurements. These fibers are very fragile and easy to break during installation and measurement. In order to understand the ultimate behavior of structures, more rugged optical fibers such as carbon/polyimide coated fibers were recently proposed. One laboratory study on two single fibers indicated that new carbon/polyimide coated fibers can sustain a maximum strain of up to 4%, which can survive any local crack in concrete members or buckling in steel members once they are installed on the structural members. This project aimed to characterize the ruggedness and signal loss of various packaged optical fibers and validate their performance as sensors. Among the tested optical fibers, bare single-mode fibers (SMF-28) with uncoated anchoring have the lowest shear strength and the lowest ultimate strain under tension, and are thus not suitable to apply in harsh environments. Polyimide-coated optical fibers have the highest shear strength and the highest ultimate strain under tension, making them the best candidate for civil infrastructure applications. Both glass fiber reinforcing polymer (GFRP) and carbon coated optical fibers are sufficiently rugged to be applied to civil infrastructure.

17. Key Words	18. Distribution Statement		
19. Security Classif. (of this report) Unclassified	20. Security Classif. (of this page) Unclassified	21. No. of Pages 70	22. Price

Table of Contents

List of Figures

List of Tables

Notations

ε_h	Strain of the host matrix
ε_a	Strain of the adhesive layer
ε_p	Strain of the packaging layer
ε_c	Strain of the optical fiber
σ_h	Stress of the host matrix
σ_a	Stress of the adhesive layer
σ_p	Stress of the packaging layer
σ_c	Stress of the optical fiber
E_h	Elastic modulus of host matrix
E_a	Elastic modulus of adhesive layer
E_p	Elastic modulus of packaging layer
E_{ap}	Elastic modulus of adhesive or packaging layer
E_c	Elastic modulus of optical fiber layer
r_h	Strain of the host matrix
r_a	Radius of the adhesive layer
r_p	Radius of the packaging layer
r_{ap}	Strain of the adhesive or packaging layer
r_c	Deformation of the optical fiber
l_f	Half-gauge length of the OFS
u_h	Deformation of the host matrix
u_a	Deformation at the end of the adhesive layer
u_p	Deformation at the end of packaging layer
u_{ap}	Deformation of adhesive or packaging layer
u_c	Deformation of the optical fiber
Δ_a	Deformation of the adhesive layer
Δ_p	Deformation of the packaging layer
B	Characteristic value of strain transfer rate of the optical fiber sensor
X	Location of the sensing point
τ	Shear stress
σ_i	Equivalent stress of the host matrix
ε_i	Equivalent strain of the host matrix
$w(\varepsilon_i)$	Damage function
G_{ap}	Shear modulus of adhesive or packaging layer
E_t	Tangential Young's modulus of the hardening portion of the host material
H	Strain transfer coefficient
k	Strain transfer error modification coefficient of OFS
w	Strain transfer error of OFS
S_z^*	Area modulus of the cross section

Acknowledgements

Financial support for this study was provided by Mid-America Transportation Center under Contract Agreement Nos. 25-1121-0001-114 and 25-1121-001-242. The authors would like to thank Jianping He, Minghua Huang, and Yuanhua Wu for their assistance with various experiments and case studies.

Disclaimer

The contents of this report reflect the views of the authors, who are responsible for the facts and the accuracy of the information presented herein. This document is disseminated under the sponsorship of the U.S. Department of Transportation's University Transportation Centers Program, in the interest of information exchange. The U.S. Government assumes no liability for the contents or use thereof.

Executive Summary

This report summarizes the findings and results of a MATC research project No. 25-1121-0001-114 and its supplemental project No. 25-1121-0001-242, which focused on rugged fiber optic sensors for large strain measurements. The objectives of this study were: a) to identify and characterize the ruggedness and strain sensing properties of optical fibers; b) to investigate optical fiber-based large-strain sensor design methods and develop packaged (coated) optical fiber sensors for the measurement of large strains in structures; and c) to apply the rugged optical fiber sensors to the measurement of large strains in various structures.

Among the tested optical fibers, bare single-mode fibers (SMF-28) with uncoated anchoring have the lowest shear strength and the lowest ultimate strain under tension, and are thus not suitable to apply in harsh environments. Polyimide-coated optical fibers have the highest shear strength and the highest ultimate strain under tension, making them the best candidate for civil infrastructure applications. Both glass fiber reinforcing polymer (GFRP) and carbon coated optical fibers are sufficiently rugged to be applied to civil infrastructure. All of the tested coated optical fibers showed satisfactory corrosion resistance in 20% NaCl solution.

The use of elastic coatings for optical fibers to improve the fiber ruggedness will not necessarily compromise the properties of the fiber sensors measured with a Brillouin Optical Time Domain Reflectometry or Analysis (BOTDR/A) system. Three mechanisms can be used to improve the ruggedness of optical fibers for large strain measurements. They include a) strain transfer with material elasticity, b) gauge length change, and c) prestressing with a polypropylene coating that significantly shrinks during material curing and thus compresses optical fibers (e.g., 12,000 με). The gauge length change mechanism is applicable to a surface attachment while the strain transfer and prestressing mechanisms are appropriate for an

internal embedment of concrete structures. The gauge length change mechanism may compromise the strain sensitivity of an optical fiber sensor since the measured strain represents the average deformation over the gauge length. The strain transfer theory developed in this study can be used to guide a practical design of large-strain optical fiber sensors. The use of a multi-layer strain transfer system may make a packaged optical fiber become bulky in practical applications. Therefore, a hybrid mechanism of reducing the strain applied on optical fibers can be very practical and effective for civil infrastructure applications. The hybrid mechanism can combine the strain transfer with material elasticity and the gauge length change for surface attachment applications or the strain transfer and the prestressing with material shrinkage for internal embedment applications. It is recommended that a hybrid strain reduction mechanism be considered in practical designs of large-strain measurements.

As validated by commercial strain gauges, both fiber Bragg gratings (FBG) and BOTDR/A optical fiber sensors can be used to accurately measure strains in civil infrastructures. Their recorded signals can be interrogated without difficulty. A single optical fiber with an FBG sensor can be used for both a point strain measurement at the location of the FBG and a distributed strain measurement along the length of the fiber using a BOTDR/A system. The two interrogation schemes can be combined to determine strain and temperature simultaneously provided the temperature variation around the FBG is very low. FRP-coated optical fibers can be integrated into various key structural components for large strain or stress measurements, such as smart cables and smart strands. A distribution monitoring technique based on coated optical fibers is highly desirable for the investigation of strain or crack distributions in large-scale concrete structures in civil engineering.

Chapter 1 Introduction

Immediately following a disastrous event such as earthquakes and hurricanes, prompt evaluations of the damage level and integrity of bridge structures are vital to emergency services and to the routine operation of an intermodal transportation network. Distributed sensors offer a cost-effective means for these evaluations. In this case, structural condition assessment often includes strain measurement and crack monitoring, both dealing with large strains.

Brillouin optical time domain reflectometry/analysis (BOTDR/A) is based on the propagation of a train of incident pulses and Brillouin back-scattering waves transmitted through an optical fiber. It is one of the most practical approaches to distributed strain sensing (Bastianini et al. 2003). The principle behind BOTDR/A is similar to that of the optical time domain reflectometry (OTDR). In OTDR, a short pulse of light is transmitted along the fiber, and the backscattered energy due to Rayleigh scattering is measured at the sending end of the fiber. The time interval between generation of the pulse and detection of the backscattering energy provides the spatial information, and the intensity of the backscattered energy provides a measure of the fiber attenuation. In a BOTDR/A system, the Rayleigh backscatter mechanism is replaced by stimulated Brillouin backscattering in which the distributed strain and temperature are related to the Brillouin frequency shift (BFS) and the Brillouin gain coefficient.

Telecom-grade optical fibers (OFs) used for Brillouin sensors can be easily damaged by vibrational, shear, and bending effects that are commonly encountered in field conditions (Chen et al. 2006). These forces can introduce the unwanted light attenuation of optical fibers if installed on rough surfaces or geometric discontinuities. One solution to this potential application issue is to integrate optical fibers into fiber-reinforced polymer (FRP) sheets to form the so-called “smart FRP tape” (Bastianini et al. 2003; Ou and Zhou 2005). Another is to strengthen the coating of optical fibers. A standard single-mode fiber such as SMF28 with an acrylate coating can sustain a maximum strain of 1~1.5% (Nikles et al. 1997). In an effort to understand

the ultimate behavior of structures, OFS Laboratories (http://www.ofsoptics.com/labs/) recently proposed the use of more rugged OFs such as carbon/polyimide coated fibers. One laboratory study of two single fibers indicated that carbon coated fibers can sustain a maximum strain of up to 4% (Zhang et al. 2007), withstanding local cracks in concrete members or buckling in steel members. One possible means to make carbon fibers more robust is to take into account their distance change due to the increased signal loss. To date, carbon optical fibers have not yet been applied to concrete structures. When optical fibers are coated or packaged, a strain transfer-induced difference develops between the optical fiber and the matrix.

This study is aimed at characterizing the ruggedness of various coated optical fibers as strain sensors in structural applications, comparing the performances of the coated optical fibers, developing several strain transfer mechanisms for large strain measurements with distributed optical fiber sensors, and developing an appropriate deployment scheme of distributed optical fiber sensors for field applications. In particular, optical Brillouin distributed sensors are required to measure large strains of transportation structures in harsh environments.

Chapter 2 Research Methodology

In this study, both analytical and experimental approaches were taken to develop and characterize rugged optical fiber sensors for distributed, large strain measurements in transportation structures. To achieve the objectives of this study, three main technical tasks were planned and executed as follows.

2.1 Ruggedness Characterization and Performance Comparison among Various Packaged (Coated) Optical Fibers

To characterize their ruggedness, various packaged optical fibers were investigated in different applications: Corning coated SM28 optical fibers, polyimide coated optical fibers, carbon coated fibers, and FRP packaged fibers. To evaluate their strength, optical fibers were tested under shear forces. To this end, a test apparatus was designed to shear optical fibers. Optical fibers were also tested for their ultimate tensile strain on a controllable platform. The sensing properties of the optical fibers were determined by collecting data with a DiTeSt STA202, a measurement system for BOTDR/A signals. To evaluate their corrosion resistance, the optical fibers were immersed in 20% NaCl (sodium chloride) solution by weight, and taken out every three months for the measurement of their strength and sensing properties. Based on the test data, the performances of various packaged optical fibers are compared for civil infrastructure applications in harsh environments.

2.2 Large-strain Sensor Development

Due to their limited deformability, bare optical fibers cannot measure the level of strains associated with the evaluation of structural safety, i.e., 2~4%. To enable large-strain measurements, an optical fiber was coated with durable materials that have a well-defined strain-transfer mechanism from the fiber to the concrete or steel member. The strain transfer theory from a damaged matrix to an optical fiber was established analytically. A prototype large-strain optical-fiber sensor based on the strain transfer theory was manufactured and tested

to its ultimate strain.

2.3 Application of Rugged Optical Fiber Sensors for Large-strain Measurements

The newly developed rugged optical fiber sensors were validated with testing of six reinforced concrete (RC) beams. Each beam was tested under a three-point load in the structures laboratory and monitored for strain with one or two optical fiber sensors. The goal was to monitor various limit states of each beam under a progressively increasing load. The recorded strains were used to identify and analyze the structural behaviors and damages such as concrete cracking, steel rebar yielding, and collapsing. After laboratory validations, the optical fiber sensors were deployed on a real-world bridge for strain measurement and field demonstration in their applicability in field conditions. Several rugged optical fiber sensors were further demonstrated for their field applications in bridge cables, prestressed steel strands, and icy soil structures.

Chapter 3 Recent Development of BOTDR/A Technology

The Brillouin scattering law was established in 1929 and experimentally verified in 1932 by French physicist Léon Brillouin. However, the Brillouin scattering phenomenon has not attracted attention in the research community of signal measurements until the late 1980s since a signal's Brillouin frequency shift is often too small to extract and process. In 1989, Horiguchi, a Japanese scholar at NTT Communications, and Culverhouse, a British scholar at the University of Kent, independently discovered that the Brillouin frequency shift of optical fibers is linearly proportional to the strain and temperature applied on an optical fiber. This finding laid down the foundation for the development of a Brillouin scattering based sensing technology, called Brillouin Optical Time Domain Reflectometry (BOTDR). Since then, the Brillouin scattering law has been well recognized and applied into the strain and temperature measurements of long-span structures. The BOTDR technology often involves the use of a common communication single-mode optical fiber that functions as both a sensing and signal transfer unit. With its outstanding sensing properties, the technology can provide the measurements of distributed strain and temperature over the entire length of a large-scale structure. The Brillouin scattering-based sensing technology also has disadvantages in practical applications. The main issues associated with this technology include measurement precision, spatial resolution, the cross sensitivity between strain and temperature measurements, and dependence on the installation method of optical fiber sensors in applications. Some of these issues are reviewed as follows.

3.1 Development of BOTDR/A Distributed Monitoring Systems

Most of the research work associated with BOTDR distributed monitoring systems are focused on the development of commercial instruments and the improvement of spatial resolution, measurement precision, sensing distance, and sampling frequency. Horiguchi (1989) pointed out that the Brillouin frequency shift of an optical fiber is linearly related to the strain

applied on the fiber. In the same year, Culverhouse et al. (1989) discovered that the frequency shift is linearly proportional to the temperature that the optical fiber experiences. The first BOTDR system was designed by Horiguchi and Kurashima (Horiguchi et al. 1990) based on the gain value of the Brillouin scattering wave. The system had a spatial resolution of 100 m and a temperature measurement precision of less than 3℃. Later on, a more advanced BOTDR/A system was designed by Bao and her associates at the University of Ottawa, Canada, based on the signal loss of the Brillouin scattering wave. For temperature measurements, the advanced system had a spatial resolution of 100 m with a sensing distance of 22 km (Bao et al. 1993). It can measure strains as small as 22 με with a spatial resolution of 5 m (Bao 1994). The system was further improved to achieve a strain measurement of 15 με with 0.5 m spatial resolution (Bao et al. 1998).

To reduce the capital cost and relax the requirement of a testing loop, Kurashima et al. (1992) investigated a single-ended measurement system with a sensing distance of 1.2 km. The latest commercial BOTDR instrument developed by NTT Communications, Japan, is the AQ8603 Model, which has a spatial resolution of 1 m, a sensing distance of 80 km and a measurement precision of ±30 με (Horiguchi et al. 1995). Fellay, a Swiss scholar, also designed a single-ended BOTDR system with a spatial resolution of less than 1 m (Fellay et al. 1997). A British University of Southampton team successfully used a Mach-Zehnder interferometer to extract the spontaneous Brillouin scattering, achieving a spatial resolution of 35 cm for temperature measurements with a temperature measurement precision of 4.3℃ (Kee et al. 2000). The University of Ottawa team presented the so-called coherent probe-pump-based sensing system, achieving the centimeter spatial resolution and high frequency resolution (Zou 2004). Due to the width and intensity of an incident pulse, further attempts to improve BOTDR/A systems have encountered technical difficulties. In theory, the narrower the width of a pulse, the higher the spatial resolution. However, a very narrow pulse makes it difficult to accurately

measure the Brillouin frequency shift accordingly. Thus, the spatial resolution of a conventional BOTDA system is practically limited to approximately 1 m in spatial resolution. The sampling rate of such a system is presently limited by the time required to sweep the probe frequency and the laser diode (LD) modulating frequency.

In recent years, several novel technologies have been proposed to improve the spatial resolution, measurement precision, and sampling rate of BOTDR/A systems. Mizuno et al. (2008) introduced a frequency-adjustable continuous wave and pump probe to produce stimulated Brillouin scattering (SBS), which is often referred to as Brillouin optical correlation-domain reflectometry (BOCDR). The probe has a spatial resolution of 1 cm and 5 cm for static and dynamic strain measurements, respectively. However, the sensing distance of this BOCDR system is too short to be useful for practical applications. The best spatial resolution and sampling rate ever reported with the Brillouin-based reflectometry technology are 13 mm and 50 Hz, respectively (Mizuno et al. 2008). The University of Ottawa team used a short pulse (~1 ns) and a pre-injected continuous wave beam as the probe beam in the pump-probe Brillouin sensor system to develop a spectrum disconsolation method (Bao et al. 2004), resulting in a spatial resolution of 1 cm. In the following year, a new system based on the pre-pulse-pump BOTDR/A (PPP-BOTDR/A) was developed. That system had a significantly improved sampling rate, a spatial resolution of 10 cm, a temperature measurement precision of 1℃ and a strain measurement precision within ±25 με (Kishida et al. 2005; Bao et al. 2005).

Of the three commercial BOTDR/A systems thus far available, the most widely used is the AQ8603 developed by NTT Communications, Japan. This system has been validated repeatedly both in laboratory and field applications. The second system, developed by Omnises, is the DiTeSt. The latest is the NXB-6000 system based on the PPP-BOTDR concept developed by NEUBREX Ltd. The AQ8603 system is used in single end measurement and is less precise than the other two systems. After nearly two decades of development, the Brillouin optical-fiber

sensing technology has reached a stage that makes it practical for large-scale structural applications. However, its sensing distance, spatial resolution, measurement accuracy, and sampling rate are still relatively low compared with other sensing devices.

3.2 Overview of BOTDA/R Sensors and their Installation Methods

The chief element of a common single-mode optical fiber is silica, which makes the optical fiber very fragile, particularly under shear deformations. As a result, without special protections, optical fiber sensors cannot be applied to engineering structures. Closely related to the fiber fragility is how optical fibers are installed in field applications. To date, it is still imperative and desirable to develop a distributed optical fiber sensor that is rugged and can be installed easily and effectively in practical applications.

Bare optical fibers were applied to sense strains, cracks, and deformation in harsh environments (Shi et al. 2000). In these cases, the optical fibers were glued to concrete or steel members. However, due to aging and creep effects, the glue has a short lifespan and becomes a serious bottleneck for the wide application of optical fibers for long-term health monitoring of engineering structures. Therefore, new packaging methods for optical fiber sensors have recently been investigated. For example, SMARTEC (http://www.roctest-group.com/products) integrated BOTDR distributed strain and temperature sensors into a thermoplastic synthetic belt and a plastic rod in the so-called SMARTape and SMARTcord, respectively, so that the optical fiber sensors are strengthened and protected in applications. SMARTEC also developed an extreme-temperature-sensing cable that consists of four single-mode or multimode optical fibers in an unstrained stainless tube and is protected by stainless steel wires or a polymer sheath (Inaudi et al. 2002 and 2003). Such sensors have been used to monitor temperature in massive concrete structures, measure strain in petroleum industrial facilities, and detect leakage in flow lines and reservoirs. The Missouri University of Science and Technology (formerly University of Missouri-Rolla) team integrated a distributed optical fiber sensor into a fiber reinforced polymer

(FRP) sheet (Bastianin et al. 2005) for distributed strain measurement. Such a "smart" FRP tape was applied to a highway bridge for strain monitoring. More recently, the Harbin Institute of Technology team has developed a Brillouin optical fiber sensor that was embedded in an FRP reinforcing bar. The "smart" FRP rebar has been applied not only in RC beams in laboratory but also in highways for strain, crack and deformation monitoring (Zhou and Ou 2007 and 2008).

To improve the spatial resolution of Brillouin optical fiber sensors, new installation schemes such as snake-like and "Ω"-like patterns were investigated. For example, Wu (2006) monitored various structures with two optical fiber attachment schemes: overall bonding method and point fixed method. They are more suitable for strain distribution and local crack detection (Wu 2006).

3.3 Temperature Compensation for Distributed Strain Measurement

Since the Brillouin frequency shift of an optical fiber is linearly proportional to a combined effect of the strain and temperature experienced by the optical fiber, a temperature change of 1°C may induce a strain of approximately 20 με, which is unacceptable in practical applications without a proper compensation. The most common technique for temperature compensation is to separate the strain measurement from the temperature measurement. Bao (1994) was the first investigator to simultaneously measure strain and temperature with a BOTDR/A system by placing two optical fibers in parallel. One fiber was installed on a structure such that it sensed temperature only, whereas the other fiber measured both temperature and strain. By comparing Brillouin frequency shifts of the two optical fibers, the strain and temperature of the structure can be determined simultaneously within 20 με and 2 °C, respectively. The Harbin Institute of Technology conducted similar studies with two parallel optical fibers to compensate temperature in strain measurements (Zhou et al. 2007).

Park (1997) discovered that the bandwidth of a Brillouin spectrum is independent of strain but varies with temperature. By measuring both the Brillouin shift and the Brillouin

bandwidth from a single optical fiber, the temperature and strain can be simultaneously obtained with a spatial resolution of 5 m. Following the Park's research, Smith et al. (1999) found that the Brillouin power is more sensitive to change in strain and temperature than the Brillouin bandwidth. Around the same time, the researchers at NTT Communications applied similar technology into the simultaneous measurement of both temperature and strain based on a BOTDR system (Kurashima et al. 1998). In 2004, the University of Ottawa team used panda, bow-tie, and tiger polarization-maintaining (PM) fibers for a simultaneous strain and temperature measurement (Bao 2004). The team found that the Brillouin power, bandwidth, and frequency shift are all linearly related to the applied strain and temperature within certain strain and temperature ranges. Thus, the temperature and the strain can be determined by any two of the three linear relationships obtained with one optical fiber: power and frequency shift, power and bandwidth, or bandwidth and frequency shift. The test results with panda PM fibers (more effective than bow-tie fibers) by Bao (2004) indicated that the use of frequency shift and power change gives a measurement precision of 8ºC for temperature and 153 με for strain, and the use of frequency shift and bandwidth change results in a measurement accuracy of 2°C for temperature and 39 με for strain. In the same year, Bao (2004) automated a BOTDR/A system with the PM fiber and photonic crystal PC fiber to further improve the spatial resolution to approximately 1 cm with a measurement precision of 10~30 με for strain and 1~2ºC for temperature.

Two interrogation schemes can be deployed on a single optical fiber for simultaneous temperature and strain measurement. For example, Davis et al. (1996) combined the fiber Bragg grating (FBG) and Brillouin scattering effects into one optical fiber measurement system for both parameters. Laboratory tests indicated that the FBG-Brillouin strategy provided a virtually distributed strain and temperature along an optical fiber with a measurement precision of 22 με and 1.9ºC, respectively. BOTDR and OTDR were also combined to determine temperature and

strain along an optical fiber (Sakairi 2002; Brown et al. 2006). The BOTDR-OTDR strategy involved a simultaneous measurement of an optical fiber's Brillouin scattering distribution (gain distribution) and Rayleigh scattering distribution (loss distribution). The strain and temperature were determined by solving two equations related to the Brillouin frequency shift measured by the BOTDR and the Brillouin scattering light power by the OTDR. Its measurement precisions for strain and temperature are ±50 με and ± 5°C with a spatial resolution of 1 m.

3.4 Application of BOTDR/A Distributed Monitoring Technology

BOTDR/A technologies have been applied to petroleum and natural gas facilities, and civil and aerospace engineering structures. The monitoring parameters in various applications include temperature, strain, deformation, and sometimes crack. Thevenaz et al. (1998) have successfully monitored a concrete dam element at Luzzone in the Swiss Alps and monitored the Lake of Geneva. For the first application, they embedded common optical fibers into the concrete structure for temperature measurement. For the second application, they laid an optical fiber over the lake bed and monitored the temperature dynamics at the bottom of the Lake. Kwon et al. (2002) installed a single 1400 m-long optical fiber on the surface of a large building for the measurement of temperature distribution. Kato et al. (2002 and 2003) monitored the failure of road slopes and the overall deformation of a large dam due to the spatial geographical environment. Another group at NTT Communications monitored telecommunication tunnels (Naruse et al. 2005), successfully detecting the tunnel deformation from 1 to 6 mm with a measurement error of 0.1 mm over a span of 10 km. In another application, Naruse et al. (2007) successfully monitored the strain distribution in one part of an existing tunnel, validating their results with a conventional method of tunnel monitoring.

Due to their light weight, durability, and capability for embedment in composites, optical fiber sensors have been applied to monitor composite structures. Shimada et al. (2000) detected damage in an advanced composite sandwich structure, an International America's Cuo Class

(IACC) yacht. The light structure was made with carbon FRP skins and a honeycomb core. From the measured strain data, the structural integrity of the IACC yacht was evaluated in real time. Yari et al. (2003) proposed a combined BOTDR and FBG system to monitor the curing process of carbon FRP laminates (Yari et al. 2003). They used the combined system to separate temperature and strain measurement, and applied a differential spectrum method to improve the system's spatial resolution. Since 2001, Shi et al. (2003, 2004, and 2005) at Nanjing University have monitored the Nanjing Gulou tunnel, Xuanwu Lake tunnel, the third Bainijing highway tunnel in Yunnan Province, China, for temperature and deformation measurements. China's Ministry of Land and Resources has established an optical fiber monitoring network to forecast mountain sliding and geological disasters in Chongqing and Wushan (Xue 2005; Zhang 2005). In 2005, researchers at Beijing Luyuan Ltd. monitored the temperature evolution in the curing process of a hydropower concrete dam in Guiyang Province. Since 2005, the Harbin Institute of Technology team has applied a combined BOTDR and FRP-packaged optical-fiber sensor to monitor the cracks in a roadway at Daqing and monitor the large strain and deformation of a civil engineering project in Guangzhou, China.

Chapter 4 Ruggedness Characterization and Performance Comparison among Various Coated Optical Fibers

4.1 Selection of Coated Optical Fibers and Experimental Methodology

Table 4.1 lists various coated optical fibers (OF) considered in this study. They were tested under shear and tensile loads to determine their ruggedness and maximum strain, respectively. In table 4.1, GFRP stands for glass fiber reinforced polymer.

During the tensile tests, the sensing properties of optical fibers can be determined using a DiTeSt STA202 measurement system for BOTDR signals. To evaluate their corrosion resistance, all optical fibers were immersed in 20% NaCl solution and taken out every three months for strength and sensing property tests. By comparing the acquired performance data of various fibers, those fibers that were sufficiently rugged for civil infrastructure applications were identified.

Table 4.1 Coated optical fibers used for ruggedness characterization and performance comparison

No.	Optical Fiber Type	Coating Material	Diameter	Manufacturer
1	Corning-SMF28	UV Acrylics	0.25 mm	Corning, Inc.
2	Polyimide Coated OF	Polyimide	0.17 mm	T&S Communications Ltd
3	Carbon coated OF	Carbon	0.17 mm	OFS Fitel, LLC
4	GFRP coated OF	GFRP	0.30 mm	Harbin Tide Science & Technology, Inc.
5	A1R05391CH1 (BI)	UV Acrylics	0.25 mm	Yangtze Optical Fiber and Cable Ltd.
6	A1R06319BF0 (BI)	UV Acrylics	0.25 mm	Yangtze Optical Fiber and Cable Ltd.
7	A9S00008CB0 (G.657)	UV Acrylics	0.25 mm	Yangtze Optical Fiber and Cable Ltd.
8	A0001952BD0(G.657)	UV Acrylics	0.25 mm	Yangtze Optical Fiber and Cable Ltd.
9	A6R06338CD0(G.657)	UV Acrylics	0.25 mm	Yangtze Optical Fiber and Cable Ltd.
10	A1R05154DC0 (BI)	UV Acrylics	0.25 mm	Yangtze Optical Fiber and Cable Ltd.

4.2 Shear Characterization of Coated Optical Fibers

To investigate the ruggedness of small coated optical fibers under shear loading, a test apparatus was custom made to cut one optical fiber at a time as illustrated in figure 4.1. The apparatus consists of a thin aluminum cutter (green color) with a small hole to hold an optical fiber, which is mechanically hinged at one end and supports a pole (blue color) at the other end for load placement, and two steel blocks (grey color) to form a narrow slot for a tight fit of the cutter. The shear force applied on the fiber can be controlled by the weight added into a pan hanging on the pole. The function of the apparatus can be simplified as shown in figure 4.2. The shear force (F) provided by the optical fiber is in equilibrium with the weight added into the pan and can thus be evaluated accordingly using the moment equation of equilibrium about the pin support (hinging point of the cutter).

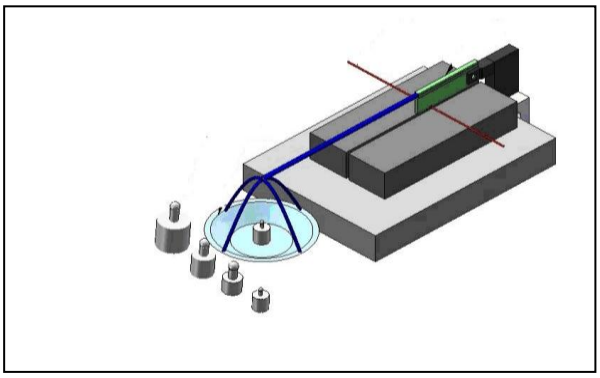

(a) Schematic design

(b) Prototype cutter

Figure 4.1 Shear loading setup

The shear strength of GFRP-coated fibers was dominated by the GFRP itself because the cross sectional area of the fiber is only 2.5% that of the GFRP with a diameter of 5 mm. For all other tests, a coated optical fiber was placed across the slot of the test apparatus with two ends glued on the top surface of the two steel blocks. Weights of various sizes were then placed in the pan progressively. Once the coated fiber was broken, the test was completed. The total load (W) can be determined from the weight set and the weight of the cutter. To ensure the repeatability of test data, at least 20 samples were tested for each type of coated fibers. Based on the test data, the average shear strength and variance were calculated for each coated optical fiber.

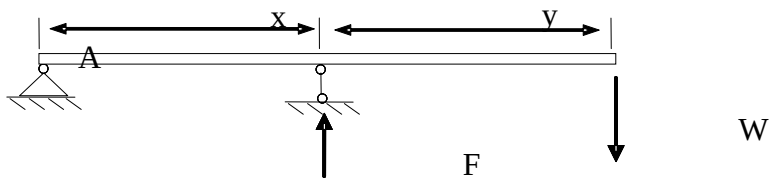

Figure 4.2 Simplified mechanical mode for optical fiber under shear loading

Except for the GFRP-coated fiber, the shear strength distribution of all samples tested for each type of coated optical fibers is presented as a plotted line graph in figure 4.3. The average shear strength and standard deviation for each type of coated fiber are summarized in table 4.2. It can be observed from table 4.2 that, except for the carbon coated fiber, the standard deviation of the sample data is all significantly below 10% of their average value, demonstrating the satisfactory consistency of the test data. The polyimide coated optical fiber had the highest shear strength, whereas the common Corning SMF had the lowest, indicating that the common single-mode fibers with no coating are especially weak. In addition, UV optical fibers coated with acrylics had low shear strength; their low shear forces are also due to their limited diameter. The shear strength and force of carbon-coated optical fibers are relatively low. The shear

strength of the GFRP-coated fiber is moderate but it can sustain the highest shear force due to its relatively large diameter. Overall, the polyimide and GFRP-coated optical fibers are considerably rugged under shear effects.

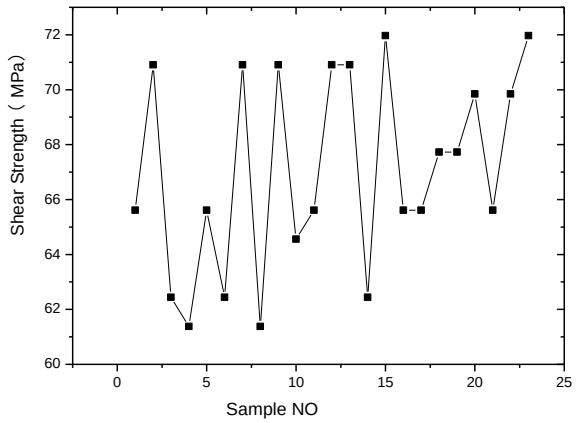

a) Corning SMF-28

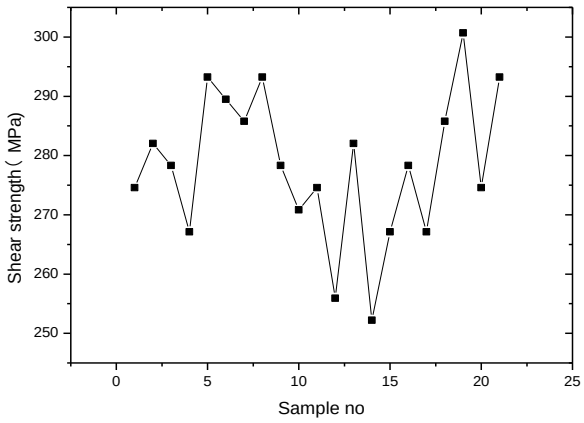

b) Polyimide coated

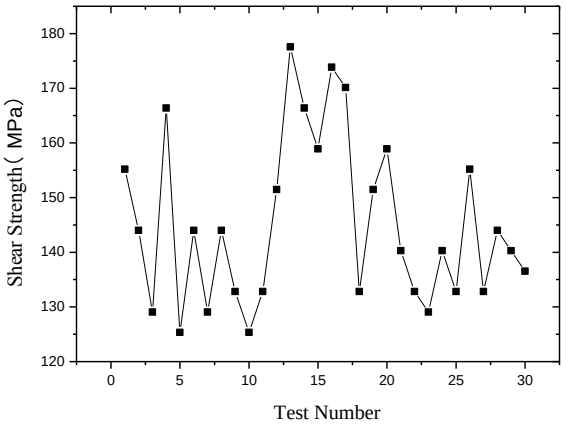

c) Carbon coated

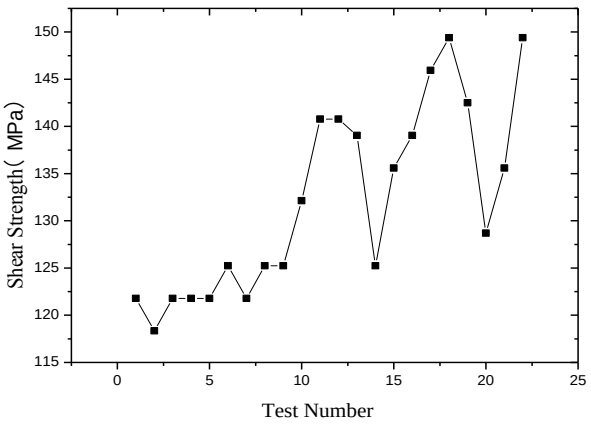

d) A1R05391CH1

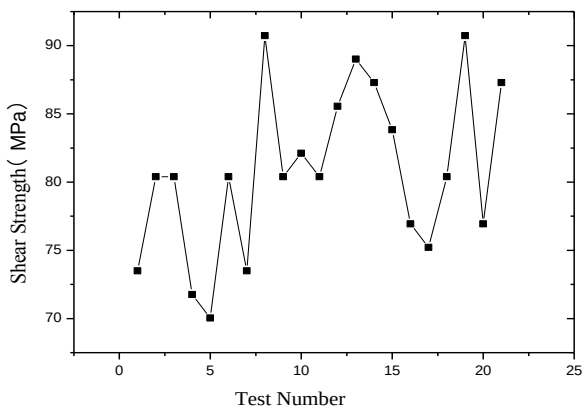

e) A1R06319BF0

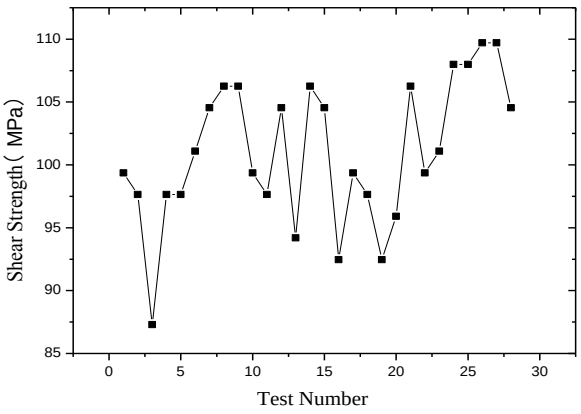

f) A9S00008CB0

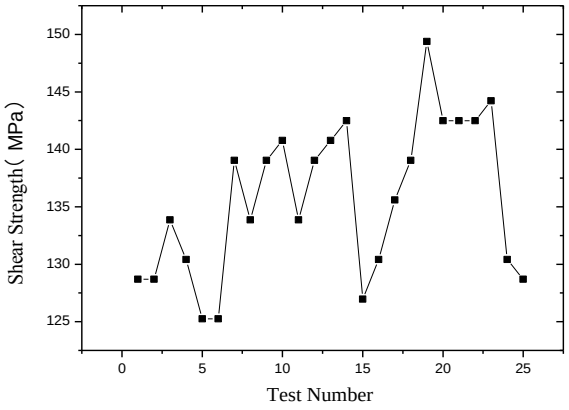

g) A0001952BD0

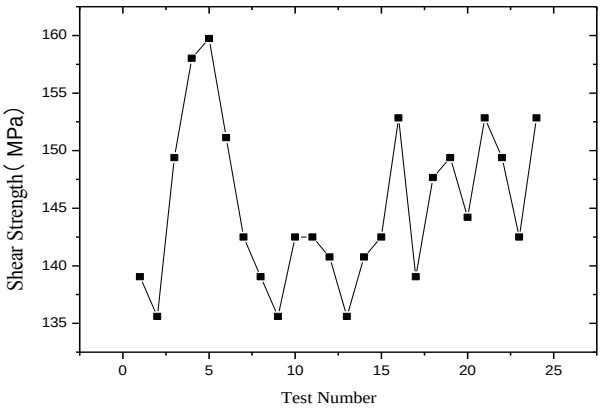

h) A6R06338CD0

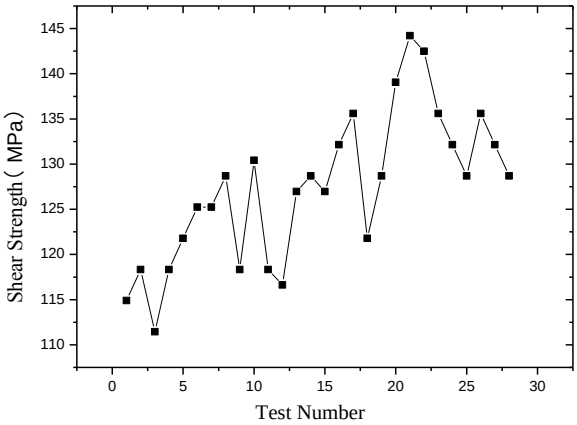

i) A1R05154DC0

Figure 4.3 Shear strength distribution of various coated optical fibers

Table 4.2 Shear strengths of various optical fibers

No.	Optical fiber type	Shear strength (MPa)	Shear strength deviation (MPa)	Coefficient of variation (%)	Shear force (N)
1	Corning-SMF28	67.04	3.53	5.27	3.29
2	Polyimide-coated	278.31	12.40	4.46	6.31
3	Carbon-coated	145.12	15.18	10.46	3.29
4	GFRP-coated	105.00	-	-	741.8
5	A1R05391CH1	80.80	6.12	7.57	3.96
6	A1R06319BF0	132.14	9.97	7.55	6.48
7	A9S00008CB0	101.03	5.27	5.22	4.96
8	A0001952BD0	135.73	6.69	4.93	6.66
9	A6R06338CD0	145.22	6.95	4.79	7.12
10	A1R05154DC0	127.39	8.31	6.52	6.25

Note: For a fair comparison with others, 3-mm-dia GFRP-coated optical fibers were tested with average shear strength of 105 MPa.

4.3 Tension Characterization of Coated Optical Fibers

4.3.1 Experimental Setup and Methodology

Because the carbon-coated fiber may be chemically the most stable, polyimide, GFRP, and carbon-coated OFs were characterized for large strain measurement under tensile tests. The widely used Corning SMF28 fiber in sensing and signal transfer was also included for comparison. Due to different sizes of the samples and different required loads to failure, two tests were set up as shown in figures 4.4(a) and figure 4.5(b), respectively. Small and large coated fibers were tested on a rolling device and a steel frame as shown in figure 4.4(b) and figure 4.5(b), respectively. The small optical fibers were directly glued on the top surface of the two rolling ends at a given gauge. The optical fibers were then extended as the two rolling ends were moving away from each other, inducing a deformation on the optical fiber. The ratio between the deformation and the gauge length is the calculated strain applied on the optical fiber. The calculated strain can be compared with the measured strain from the BOTDR/A system. Since large GFRP packaged optical fibers cannot be easily extended over a long gauge (i.e. 1.0 meter), a steel frame was built to facilitate the tests. The GFRP-coated optical fibers can be loaded with a hydraulic pump. The extension of the GFRP-coated optical fibers can be measured

by an extensometer and by the BOTDR/A system. Different types of glues and various anchoring lengths were considered during tests as discussed below.

a) Experimental setup

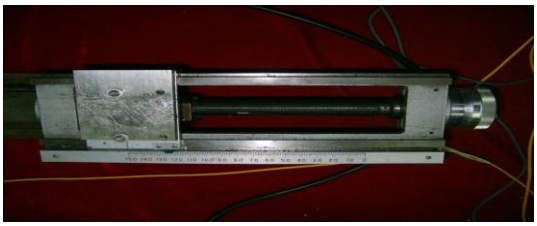

b) Rolling device for loading

Figure 4.4 Testing of small coated optical fibers under tension

a) Experimental setup

b) Steel frame for loading

Figure 4.5 Testing of large coated optical fibers under tension

4.3.2 Sensing Property and Ultimate Strain of SMF28 Optical Fibers

SMF-28 optical fibers were set up in various anchoring lengths with the 502 glue, a type of acrylic acid glue that dries easily on strain gauges. For comparison, two anchoring methods of different lengths were used for bare SMF-28 optical fibers: one anchored with coating over a 5 cm base length and the other anchored without coating over a 17 cm base length. Figure 4.6 presents the relationship between BFS and the applied strain of each SMF-28 optical fiber with coated anchors. It can be observed that the BFS-strain curve up to a strain of 14,000με is basically linear. Indeed, a linear regression analysis indicated that the correlation coefficient

exceeded 0.9995 for each curve. The slope of the BFS-strain curve is defined as the strain coefficient of the tested fiber in MHz/με. The ultimate strain of the SMF28 fiber with coated anchors was defined as the strain corresponding to the maximum BFS. It can also be observed from figure 4.6 that the BFS nonlinearly increases with the applied strain ranging from 14,000με to the ultimate strain, and then suddenly drops to a much smaller value. This observation indicated that the coating material at anchors is increasingly deformed to the maximum extent and then gradually debonded from the optical fiber. As a result of the debonding induced slip between the coating at anchors and the optical fiber, the BFS decreased after the ultimate strain.

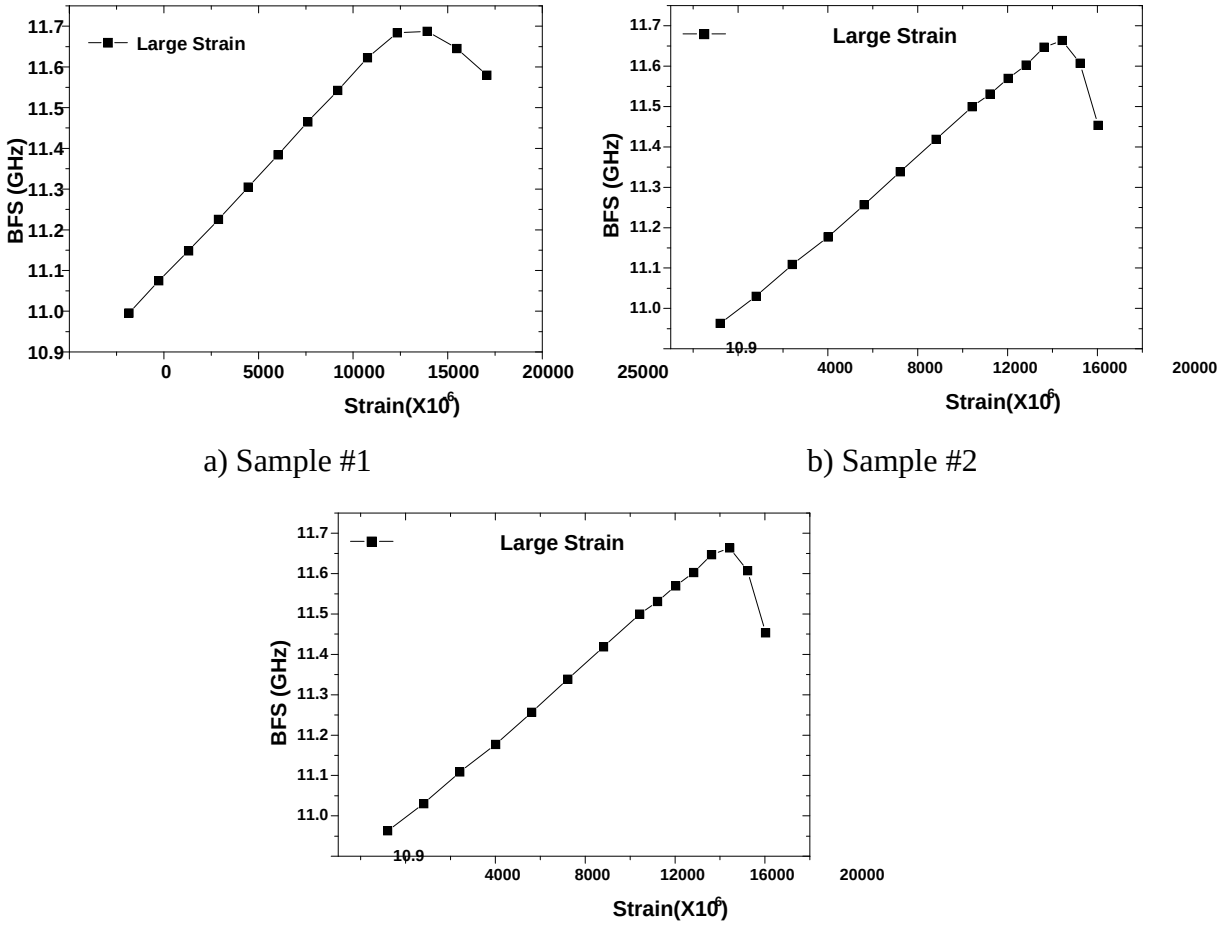

a) Sample #1

b) Sample #2

c) Sample #3

Figure 4.6 Relationship between BFS and strain of coated SMF28 optical fibers

Table 4.3 lists the strain coefficient and the ultimate strain of each optical fiber with

coated anchors. Table 4.4 lists the ultimate strain of each optical fiber with uncoated anchors. Tables 4.3 and 4.4 demonstrate that the strain coefficients of SMF28 optical fibers are consistent among all test samples. The ultimate strains of optical fibers with uncoated anchors occurred when the fibers broke. The difference in ultimate strain between the coated and uncoated anchors, listed in tables 4.3 and 4.4, indicates that the measured strains were significantly increased due to a strain transfer mechanism from the anchor coating to the core of the optical fibers. Therefore, coating can be a viable approach to enhance the strain measurement range of optical fiber sensors in practical applications.

Table 4.3 Strain coefficient and ultimate strain of SMF28 optical fibers with coated anchors

Sample	Strain coefficient ($MHz/\mu\varepsilon$)	Ultimate strain ($\mu\varepsilon$)	Anchoring length (cm)	Damage
1	0.495	16800	5	Slipping
2	0.480	18300	5	Slipping
3	0.483	17600	5	Slipping

Table 4.4 Ultimate strain of SMF28 optical fibers with uncoated anchors

Sample	Ultimate strain ($\mu\varepsilon$)	Anchoring length (cm)
1	11700	17
2	11300	17
3	10200	17
4	10500	17
5	12000	17

4.3.3 Sensing Property and Ultimate Strain of Polyimide-coated Optical Fibers

Polyimide-coated optical fibers were tested under tension with 5 cm and 17 cm anchoring lengths. The 502 glue was also used to attach each optical fiber to the test apparatus. Figure 4.7 shows the linear portion of the BFS-strain curves for three tests. Table 4.5 lists the strain coefficient and ultimate strain of each test. All three samples eventually failed in debonding of polyimide coating from the optical fiber based on the visual observation of slipping.

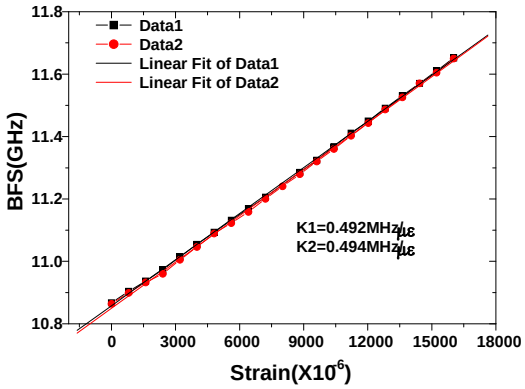

a) Sample #1

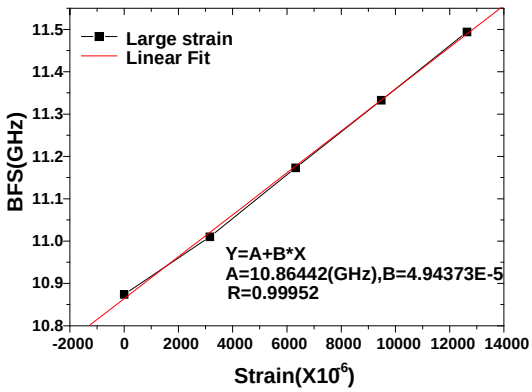

b) Sample #2

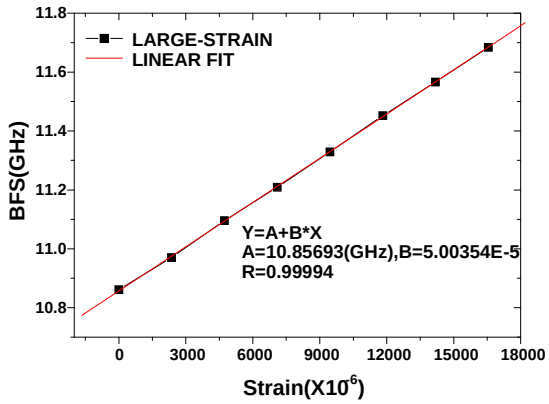

c) Sample #3

Figure 4.7 Relationship between BFS and strain of polyimide-coated fibers with 502 glue

Table 4.5 Sensing property and ultimate strain of polyimide-coated fibers with 502 glue

Sample	Strain coefficient (MHz/με)	Ultimate strain (με)	Anchoring length (cm)	Damage
1	0.497	35500	5	
2	0.494	56600	17	Slipping
3	0.500	55400	17	

To understand the role that adhesives play in strain transfer, epoxy resin was also used to attach polyimide-coated optical fibers over a 17 cm anchoring length. Table 4.6 lists the ultimate

strain and damage state of test samples. Here the damage state is defined as optical fiber breakage or slippage from the adhesives. These tests confirmed that, prior to optical fiber damage, the BOTDR/A system performed well with good quality signals even when optical fibers were subjected to large strains. In general, the ultimate strain of polyimide-coated optical fibers can reach approximately 40,000 με provided that the anchoring holds. However, the ultimate strains from various samples are quite inconsistent likely due to non-uniform materials. For practical applications, the minimum anchoring length should be specified for a given adhesive.

Table 4.6 Ultimate strain and damage state of polyimide-coated fibers with epoxy resins

Test	Sample	Ultimate strain ($\mu\varepsilon$)	Signal quality	Anchoring length (cm)	Damage state
1	a	27300	Good	17	Debonding
	b	33100			
	c	39200			
2	a	39000	Good	17	Broken
	b	56500			
	c	48200			
3	a	39800	Good	17	Broken
	b	51000			
	c	53700			

To ensure their long-term behavior at high strain levels, a polyimide-coated optical fiber was repeatedly loaded and unloaded to the same level of the applied strain. The strain measured with the BOTDR/A system corresponding to the initial strain applied is a function of the number of cycles as shown as a plotted line graph in figure 4.8. In general, the strain measurements are stable around the initial strain value. This observation indicates that the long-term behavior of optical fibers with the BOTDR/A measurement system is reliable.

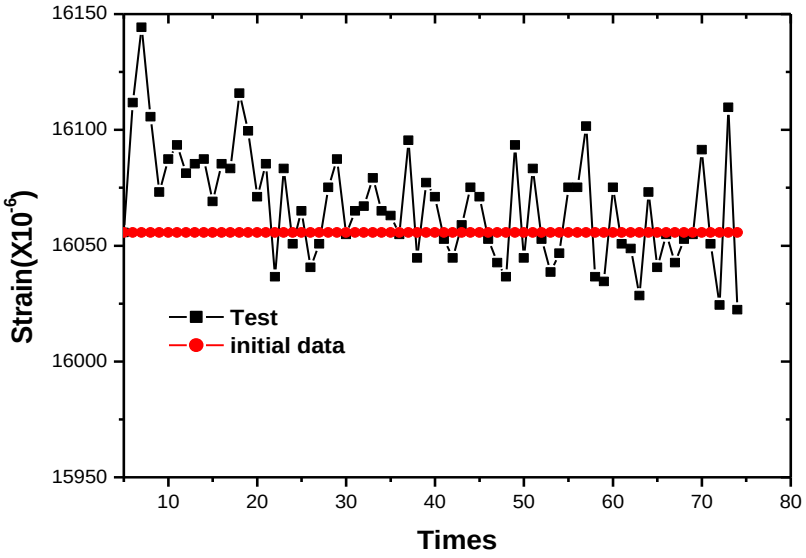

Figure 4.8 Long-term monitoring of optical fibers at large stress

4.3.4 Sensing Property and Ultimate Strain of Carbon-coated Optical Fibers

Figure 4.9 shows the linear portion of the BFS-strain curves for four carbon-coated optical fiber samples. In this case, the carbon-coated optical fibers were attached to the test apparatus with the J39 glue. All test samples eventually failed in debonding of the glue.

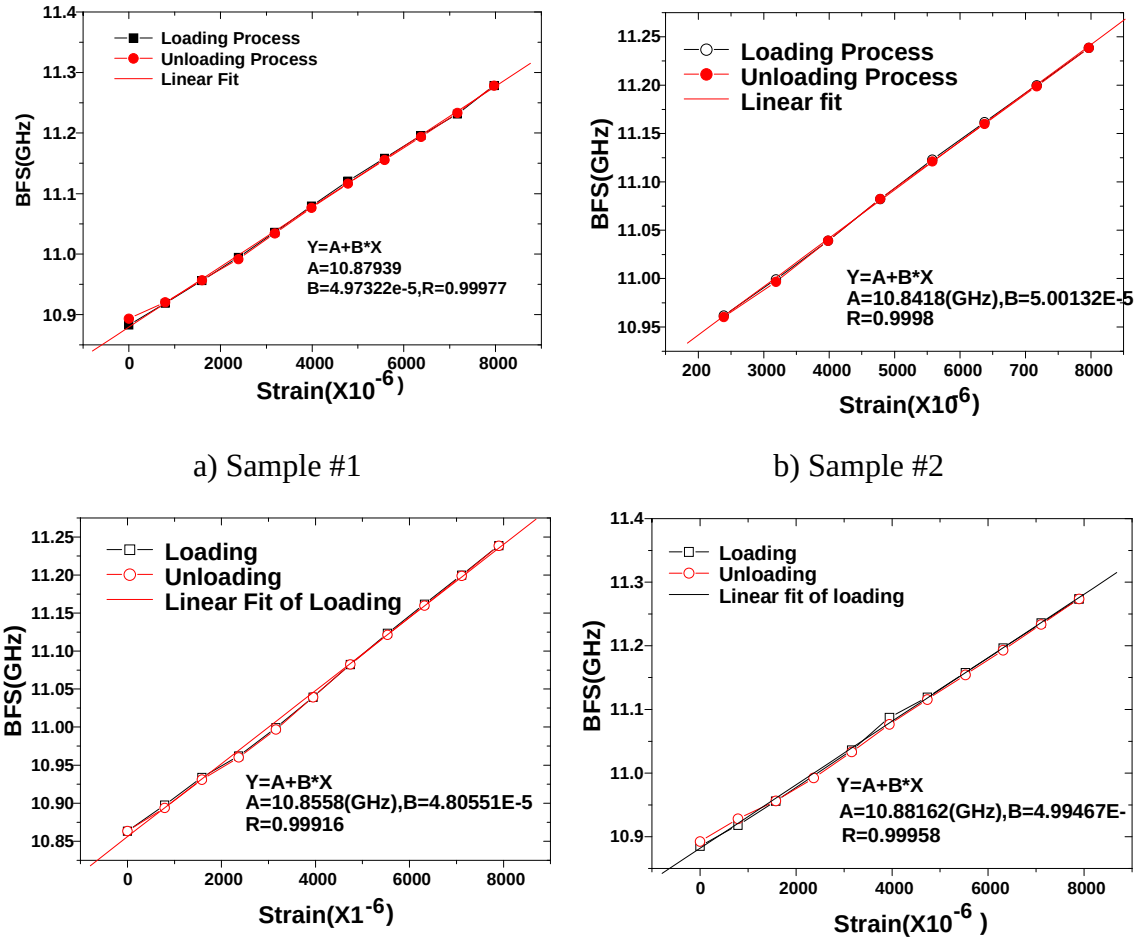

a) Sample #1 b) Sample #2

c) Sample #3 d) Sample #4

Figure 4.9 Relationship between BFS and strain of carbon-coated fibers with J39 glue

The sensing property and ultimate strain of the carbon-coated optical fibers are given in table 4.7. Similarly, epoxy resin was also used to test the ultimate strain of the carbon-coated fibers. The test results with the epoxy resin are presented in table 4.8. These results indicate that the carbon-coated optical fibers have a high sensitivity to strain effects until damage occurs. The optical fibers are sufficiently rugged to withstand over 30,000 με provided they are adequately anchored. Comparison of table 4.7 and table 4.8 demonstrates that if the optical fibers are not completely fixed with the glue over the anchoring length, test results may be inconsistent, depending largely on the flexibility of the support.

Table 4.7 Sensing property and ultimate strain of carbon-coated fibers with J39 glue

Sample	Strain coefficient (MHz/με)	Ultimate strain (με)	Anchoring length (*cm*)	Damage
1	0.500	44800	17	Slipping
2	0.497	45000		
3	0.481	44400		
4	0.499	42600		

Table 4.8 Ultimate strain of carbon-coated fibers with epoxy resin

Sample	Ultimate strain ($\mu\varepsilon$)	Anchoring length (cm)	Damage
1	30900	17	Broken
2	32100		
3	32800		

4.3.5 Sensing Property and Ultimate Strain of GFRP-coated Optical Fibers

The GFRP-coated fibers were tested on the steel frame setup as shown in figure 4.5. Figure 4.10 shows the linear portion of the BFS-strain curves as plotted line graphs for two samples. All test samples eventually broke. Table 4.9 lists the sensing property and ultimate strain of the samples. The test results reveal that the sensing property was quite consistent before the fibers broke with no slip between them and the GFRP. The ultimate strain is approximately 20,000 $\mu\varepsilon$.

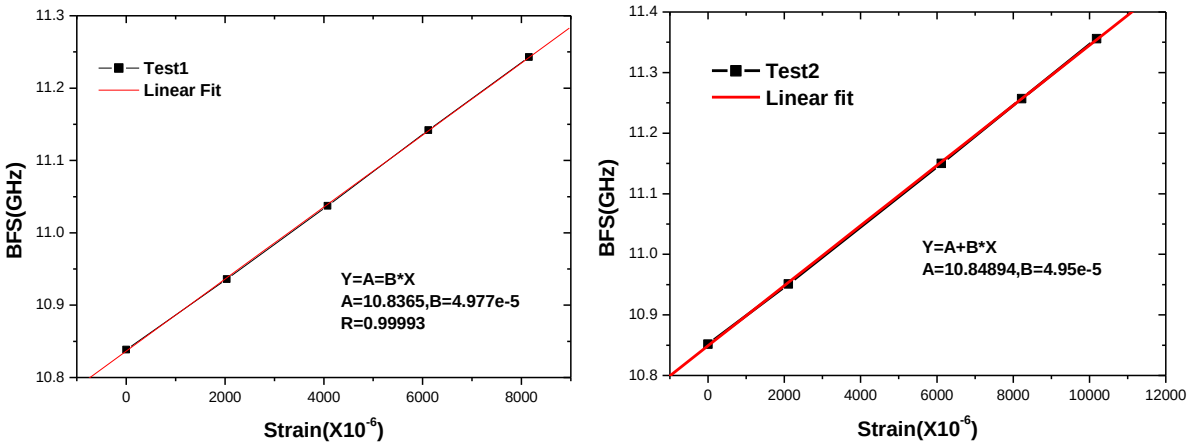

a) Sample #1 b) Sample #2

Figure 4.10 Relationship between BFS and strain of GFRP-coated optical fibers under tension

Table 4.9 Sensing property and ultimate strain of GFRP-coated optical fibers

Sample	Strain coefficient (MHz/με)	Ultimate strain (με)	Anchoring length (cm)	Damage
1	0.497	20700	30	Broken
2	0.495	20000	30	Broken

4.3.6 Comparison of Sensing Properties and Ultimate Strains of Selected Optical Fibers

Table 4.10 compares the average sensing property and ultimate strain of each type of tested samples with the same damage state. It clearly indicates that all the sensing properties are consistent and close to that of bare optical fibers. However, the ultimate strains of various optical fibers vary considerably, depending upon their damage states and the selected anchoring lengths. In practice, the anchoring length for an optical fiber must be ensured large enough to prevent the fiber from damage in specified application ranges. Furthermore, the use of coating can significantly change the strain transfer from the matrix to the optical fiber. Like the shear strength, the ultimate strain of polyimide-coated optical fibers is the highest, making it most suitable for large strain measurement in practical applications. Carbon and GFRP-coated optical fibers are acceptable sensors for distributed strain measurement of civil infrastructure.

Table 4.10 Summary of average sensing properties and ultimate strains of optical fibers

Coating type	Anchoring adhesive	Anchoring length (cm)	Ultimate strain (με)	Strain coefficient (MHz/με)	Damage
SMF28	502 with coating	5	17500	0.486	Slipping
	502 without coating	17	11100	-	Broken
Polyimide	502	5	35500	0.497	Slipping
		17	56000	0.497	Slipping
	Epoxy resin	17	33200	-	Debonding
			48100	-	Broken
Carbon	J39	17	44200	0.494	Slipping
	Epoxy resin		31900	-	Broken
GFRP	-	-	20400	0.486	Broken

4.4 Ruggedness of Coated Optical Fibers in Corrosive Environment

GFRP-coated and other optical fibers were immersed in 20% NaCl solution as shown in figure 4.11(a) and (b), respectively. Each sample was taken out every 3 months for the testing of fiber strength. Tables 4.11 and 4.12 summarize the shear strength and ultimate strain of various coated optical fibers after corrosion. It can be observed from tables 4.11 and 4.12 that the mechanical strength of the optical fibers shows no obvious sign of degradation after the corrosion tests up to nine months. This result is attributable to the high corrosion resistance of optical fibers in the NaCl solution. Based on the above test results, it can be concluded that all the coated fibers tested in this study can satisfactorily withstand corrosion in 20% NaCl solution.

a) Setup of GFRP-coated optical fibers

b) Setup of small optical fibers

Figure 4.11 Corrosion tests of coated optical fibers

Table 4.11 Shear strength of various optical fibers after corrosion tests

No.	Optical fiber type	Diameter (μm)	Shear strength (MPa)		Shear Force	
			3 month	6 month	3 month	6 month
1	Corning SMF28	250	109.65	124.74	5.38	6.12
2	Polyimide-coated	170	269.32	309.88	6.11	7.03
3	Carbon-coated	170	194.39	192.57	4.41	4.38
4	A0001952BD0	250	110.88	120.87	5.44	5.93

Table 4.12 Ultimate strain of various optical fibers after corrosion tests

Coating type	Adhesive	Anchoring Length (cm)	Ultimate Strain (με)			Damage
			3 month	6 month	9 month	
GFRP			19300	20200	20212	Broken
Polyimide	J133	17	45000	47500	46640	Broken
Carbon	J133	17	44300	39700	45700	Broken
	502	17	11000	13400	9700	Broken
SMF-28	J133	17	26000	22400	23500	Broken
	Epoxy resin	17	18000	21000	23000	Slipping

Chapter 5 Large-strain Sensor Development

This report analyzes the mechanism of strain transfer between an optical fiber sensor and the matrix, and it explains the design of the large-strain optical fiber sensor. Further, it describes three methods of optical fiber sensors for large strain measurement: strain transfer with material elasticity, gauge length change, and prestressing with material shrinkage. To verify these mechanisms, long-period fiber gratings (LPFG) and fiber Bragg gratings (FBG) were tested for each sensor development method.

5.1 Large-strain Optical Fiber Sensors Based on Strain Transfer Theory

5.1.1 General

With the rapid development of optical fiber sensing technology, optical fiber sensors such as fiber optical grating sensors (e.g., FBG, LPFG), BOTDR/A, and Fabry-Perot sensors have become widely accepted for field applications, especially in communications, computer, aerospace and civil engineering. However, despite their field applications, fundamental studies of optical fiber sensors are still needed. Among various issues to be addressed, strain transfer analysis and sensing error modification based on the theory of strain transfer are among the most important, and these have attracted considerable attention in recent years. Much research on composite materials, for example, has focused on the analysis of strain (stress) transfer analysis among various layers. The current most commonly used strain transfer theory is derived from the shear lag theory proposed in 1952 by Cox. The shear lag theory states that under axial loading condition, shear stress develops due to the difference between the Young's modulus of the host matrix and the inserted fiber. The transfer of stress from the host matrix to the fiber is completed by this particular form of shear stress. Based on the shear lag theory, the strain transfer of an optical fiber sensor can be analyzed for both embedded and adhered conditions.

Analysis model and basic assumptions. One common model of strain transfer analysis for optical fiber sensors is based on the cylindrical model shown as a diagram in figure 5.1. It has

two basic assumptions based on shear lag theory. First, all the materials used are isotropic, elastic, and homogenous in all directions. Second, the interfaces between layers are perfect with no sliding or stripping. In addition, the temperature effect is negligible.

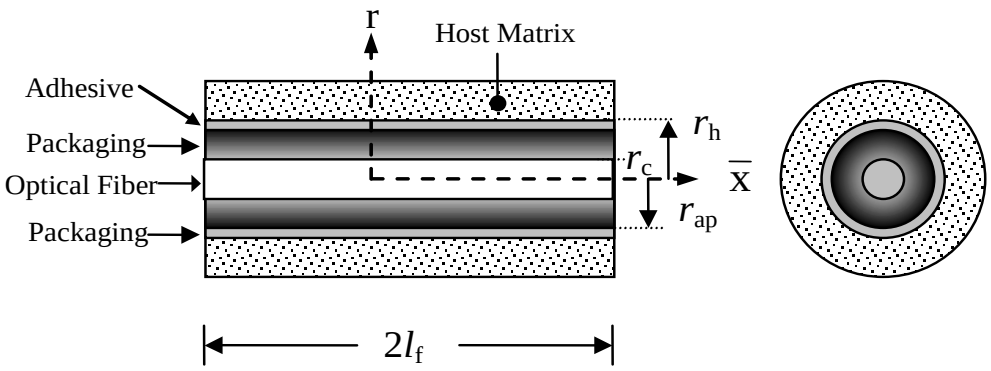

Figure 5.1 Cylindrical model of optical fiber strain sensing

Based on the first assumption, the linear theory of mechanics is considered. In this case, the stress-strain relation or the constitutive law of the materials can be expressed as

$$\varepsilon_h(\bar{x}) = \frac{\sigma_h(\bar{x})}{E_h},\ \varepsilon_a(\bar{x}) = \frac{\sigma_a(\bar{x})}{E_a},\ \varepsilon_p(\bar{x}) = \frac{\sigma_p(\bar{x})}{E_p},\ \varepsilon_c(\bar{x}) = \frac{\sigma_c(\bar{x})}{E_c} \tag{5.1}$$

where ε_h, ε_a, ε_p, and ε_c are strain of the host matrix, adhesive layer, packaging layer, and the optical fiber, respectively; σ_h, σ_a, σ_p, and σ_c are stress of the host matrix, adhesive layer, packaging layer, and the optical fiber, respectively; E_h, E_a, E_p, and E_c are the elastic modulus of each layer.

Based on the second assumption, the deformation relationship of the cylindrical model can be expressed as

$$\begin{cases} u_{\mathrm{c}}(\bar{x}) = u_{\mathrm{p}}(r_{\mathrm{c}}, \bar{x}) & r = r_{\mathrm{c}} \\ u_{\mathrm{p}}(r_{\mathrm{ap}}, \bar{x}) = u_{\mathrm{a}}(r_{\mathrm{ap}}, \bar{x}) & r = r_{\mathrm{ap}} \\ u_{\mathrm{a}}(r_{\mathrm{h}}, \bar{x}) = u_{\mathrm{h}}(\bar{x}) & r = r_{\mathrm{h}} \end{cases} \tag{5.2}$$

where

$$u_{\mathrm{h}}(\bar{x}) = \Delta_{\mathrm{a}}(\bar{x}) + \Delta_{\mathrm{p}}(\bar{x}) + u_{\mathrm{c}}(\bar{x})$$
$$\Delta_{\mathrm{a}}(\bar{x}) = u_{\mathrm{a}}(r_{\mathrm{h}}, \bar{x}) - u_{\mathrm{a}}(r_{\mathrm{a}}, \bar{x}_{\mathrm{p}})$$
$$\Delta_{\mathrm{p}}(\bar{x}) = u_{\mathrm{p}}(r_{\mathrm{ap}}, \bar{x}) - u_{\mathrm{p}}(r_{\mathrm{p}}, \bar{x}_{\mathrm{c}})$$

These deformation relationships can be illustrated as a diagram in figure 5.2.

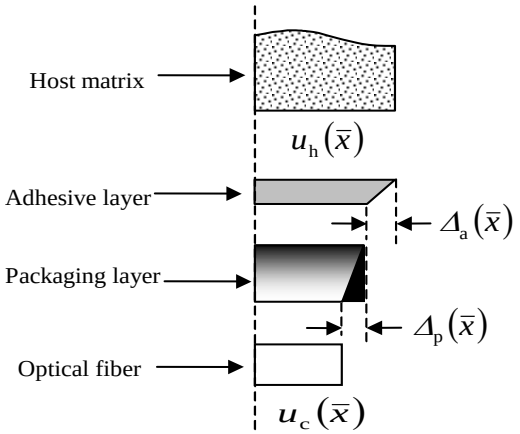

Figure 5.2 Deformation relationship for the cylindrical model

Force equilibrium analysis of optical fiber sensor. Because the optical fiber sensors are insensitive to transverse stress, this work considered only the longitudinal normal stress and shear stress. Based on the free-body diagram of the optical fiber as shown in figure 5.3, the following equations can be derived:

$$\frac{\mathrm{d}\sigma_{\mathrm{c}}(\bar{x})}{\mathrm{d}\bar{x}} = -\frac{2\tau_{\mathrm{pc}}(r_{\mathrm{c}}, \bar{x})}{r_{\mathrm{c}}} \tag{5.3}$$

where τ is the shear stress.

Based on the free-body diagram of the packaging layer as shown in figure 5.4 and the force equilibrium along the x axis, the following relationship can be derived:

$$\frac{\mathrm{d}\sigma_{\mathrm{p}}(\bar{x})}{\mathrm{d}\bar{x}} = \frac{2[\tau_{\mathrm{pc}}(r_{\mathrm{c}}, \bar{x})\ r_{\mathrm{c}} - \tau(r_{\mathrm{ap}}, \bar{x})\ r_{\mathrm{ap}}]}{r_{\mathrm{ap}}{}^2 - r_{\mathrm{c}}{}^2} \tag{5.4}$$

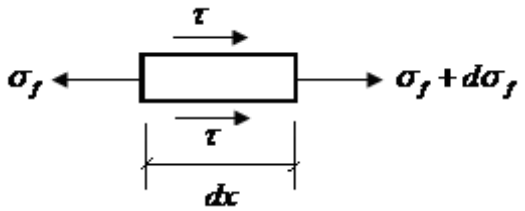

Figure 5.3 Free-body diagram of the optical fiber

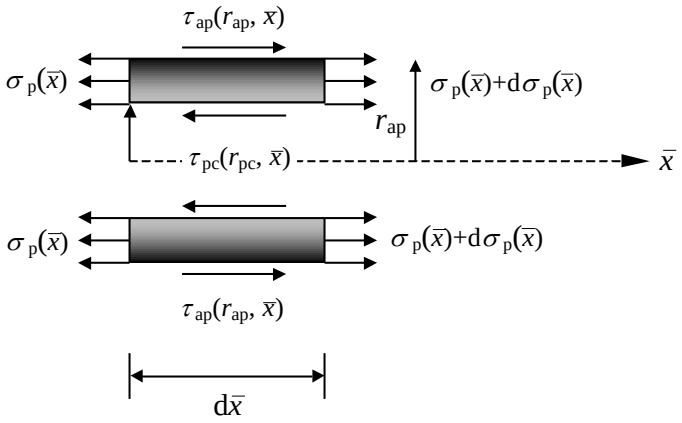

Figure 5.4 Free-body diagram of the packaging layer

Assuming that the optical fiber is engaged in the bending condition, the normal stress of the host matrix can be given as

$$\frac{\mathrm{d}\sigma_{\mathrm{h}}(\bar{x})}{\mathrm{d}\bar{x}} = \frac{\tau(r_{\mathrm{h}}, \bar{x})\ by}{S_{\mathrm{z}}^{*}} \tag{5.5}$$

where S_z^* is the area modulus of the cross section.

By combining equations (5.1) - (5.4) and considering the compatibility of multiple layers, the differential equation governing the shear stress is:

$$\frac{\partial \tau_{\mathrm{ap}}{}^{2}(r_{\mathrm{ap}}, \bar{x})}{\partial^2 \bar{x}} - \beta^2 \tau_{\mathrm{ap}}(r_{\mathrm{ap}}, \bar{x}) = 0 \tag{5.6}$$

where β is the characteristic value of the sensor' strain transfer rate and it can be expressed as

$$\beta_1^{\,2} = \frac{2}{E_0 r_0^{\,2} \sum_{i=1}^{n} \left(\frac{1}{G_i} \cdot \frac{r_i}{r_{i-1}} \right)} \quad \text{for short OFS and multi-layers and}$$

$$\beta_2^{\,2} = \frac{\frac{2}{E_0 r_0^{\,2}} + \frac{by}{E\ S_{\mathrm{n}}^{*} r_{n}}}{\sum_{i=1}^{n} \left(\frac{1}{G_i} \cdot \frac{r_i}{r_{i-1}} \right)} \quad \text{for long OFS and multi-layers.}$$

Solutions and discussion. Equation (5.6) can then be solved for:

$$\tau_{\mathrm{ap}}(r_{\mathrm{ap}}, \bar{x}) = \frac{\sigma_{\mathrm{c}} r_{\mathrm{c}}^{\,2} \beta}{2 r_{\mathrm{ap}} \sinh(\beta l_{\mathrm{f}})} \cosh(\beta l_{\mathrm{f}}) \tag{5.7}$$

$$\varepsilon_{\mathrm{c}}(\bar{x}) = \varepsilon_{\mathrm{c}} \left[1 - \frac{\sinh(\beta \bar{x})}{\sinh(\beta l_{\mathrm{f}})} \right] \tag{5.8}$$

Equations (5.6) and (5.7) demonstrate that the sensor's strain transfer rate depends highly on several parameters: $E_0, E_h, G_i, r_0, r_h, r_i$, and l_f. This dependence means that not only the packaging material, but also the host matrix material and its damage type and extent can influence the strain transfer rate of the sensor. In the large strain stage, most of the host matrix is nonlinear or plastic. This plasticity of the host matrix functions as a kind of damage of the host matrix and thus affects the strain transfer rate of the sensor. Therefore, the development of an optical fiber sensor for large strain measurement must consider appropriate strain transfer analysis taking into account the plasticity of the host matrix.

5.1.2 Strain Transfer Mechanism with Consideration of Plastic Damage in Host Matrix

Since catastrophic disasters recently occur more frequently and cause greater damage, the structural safety of critical constructed facilities has recently come to the forefront of most research worldwide. Structures often experience inelastic deformation, and they are subjected to strains beyond their yield point. For the purpose of safety assessment, the measurement of large strains is becoming increasingly important.

The analysis presented in this section is based on a cylindrical model in a host matrix with a diameter of r_h subjected to a uniform tension stress at both ends. One optical fiber sensor is embedded along the center of the cylinder over its mid-point. Figure 5.5 shows a diagram of half of the cylinder model. The model is symmetrical about the origin of the x-axis, which is located at the mid-point of the cylinder. Here, r_c is the outer radius of the optical fiber, and r_{ap} is the outer radius of the package layer, and the term $\pm\sigma_0$ is the external uniform stress applied on the cylinder; the positive sign indicates that it is in tension and the negative sign indicates it is in compression. Due to symmetry, the cross section of the host matrix and the optical fiber is subjected to zero shear stress and thus to uniform axial stress at the mid-point of the cylinder.

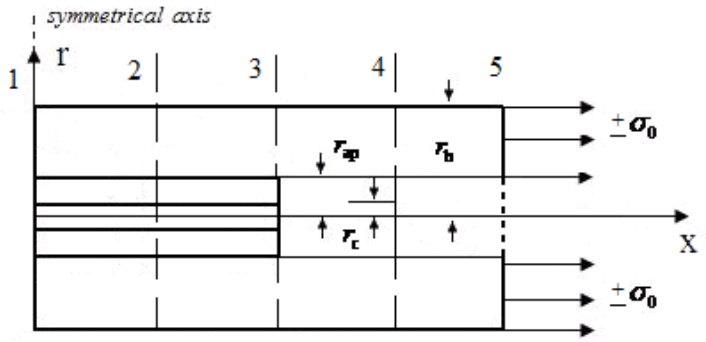

Figure 5.5 Half of the cylinder

The following derivation rests on three assumptions:

(1) The optical fiber and packaging materials are elastic.

(2) The host matrix and the optical fiber are perfectly bonded.

(3) The optical fiber (<125 μm in diameter) is subjected to strain through the dominant shear action of package materials with negligible axial stress at each end (because r_c/r_h is typically in the order of less than 10^{-2}).

According to the plastic deformation theory, the general constitutive law of host materials can be expressed as

$$\sigma_i = E_h[1 - w(\varepsilon_i)]\varepsilon_i \tag{5.9}$$

where σ_i and ε_i are the stress and strain of the host matrix, respectively, E_h represents the Young's modulus of the host material at low strain, and $w(\varepsilon_i)$ is a damage function that takes different forms for various materials.

For exponent hardening materials such as high strength steel, $w(\varepsilon_i)$ can be written as

$$w(\varepsilon_i) = 1 - \frac{A\varepsilon_i^{n-1}}{E_h} \quad . \tag{5.10}$$

For low carbon steel, a bilinear hardening stress-strain relationship can be used to model the material behavior. In this case, the damage function in equation (5.9) can be expressed as

$$w(\varepsilon_i) = \left(1 - \frac{E_t}{E_h}\right)\left(1 - \frac{\varepsilon_s}{\varepsilon_i}\right) \quad . \tag{5.11}$$

where E_t is the tangential Young's modulus of the hardening portion of the host material.

Thus, taking into account the plastic deformation in the host material, the strain transfer relationship between the host matrix and the optical fiber in equation (5.7) can be modified as

$$\varepsilon_c(x) = \eta \varepsilon_h(x) \tag{5.12}$$

The strain transfer rate (STR) η is calculated as

$$\eta = 1 - \frac{\cosh(\beta_{c1} x)}{\mathrm{osh}(\beta_{c1} l_f)} - \frac{\cosh(\beta_{ap1} x)}{\left(1 - \dfrac{E_c E_h r_c \left[1 - w(\varepsilon_i)\right]}{3E_{ap} G_{ap}(r_h - r_{ap})}\right)\cosh(\beta_{ap1} l_f)} \tag{5.13}$$

where

$$\beta_{ap1}^2 = \frac{4E_h\left[1 - w(\varepsilon_i)\right]}{3E_{ap}(r_h - r_{ap})r_{ap}} \tag{5.14}$$

and

$$\beta_{c1}^2 = \frac{4G_{ap}}{E_c(r_{ap} - r_c)r_c} \quad . \tag{5.15}$$

To simplify equation (5.13) for practical applications, r_c / r_h can be considered to be approximately zero because the optical fiber is small in diameter. Since this study focuses

primarily on the effects of plastic deformation in the host matrix, the strain from the packaging material and the optical fiber is assumed to be equal at their interface. Equation (5.13) can then be simplified into

$$\eta = 1 - \frac{\cosh\left(\beta_{ap1} x\right)}{\cosh\left(\beta_{ap1} l_f\right)} \quad . \tag{5.16}$$

Considering zero or positive *x* for the half of a cylinder， $\cosh\left(\beta_{ap1} x\right)$ is a monotonically increasing function and $\cosh\left(\beta_{ap1} x\right)\left[\cosh\left(\beta_{ap1} l_f\right)\right]^{-1}$ decreases as β_{ap1} increases. Therefore, the maximum value of the strain transfer rate η occurs at the maximum value of β_{ap1} and x=0.

Once η is known, the modified strain of the host matrix can then be determined from the strain in the optical fiber sensor by:

$$\varepsilon_h = k\varepsilon_c \, . \tag{5.17}$$

where the modification coefficient k is equal to:

$$k = \frac{1}{\eta} = 1 + \frac{\cosh\left(\beta_{ap1} x\right)}{\cosh\left(\beta_{ap1} l_f\right) - \cosh\left(\beta_{ap1} x\right)} . \tag{5.18}$$

However, the modification coefficient, *k*, is implicitly related to the characteristics parameter of the host matrix β_{ap1}, which is in turn a function of ε_h. Therefore, numerical iterations must be performed to get the solution of *k*. When the host matrix is concrete and the packaging material is FRP material, the ratio of the Young's moduli between the host matrix and the packaging material is approximately 0.435. Furthermore, the dimensions of the host matrix

and the optical fiber sensor can be selected as follows. The ratio of the radii between the host matrix and the packaging material is approximately 10. The radius of the packaging layer is 2.5 mm, and the length of the sensor is 100 mm. For this case, figure 5.6 shows in a plotted line graph the plastic damage as a function of strain. The damage function $w(\varepsilon_i)$ reaches 0.5 and 0.7 as the strain increases to 0.165%, and 0.23%, respectively.

Figure 5.7 shows a three-dimensional presentation of the strain transfer rate as a function of strain and location. It can be seen that at various strain levels and sensor locations, the strain transfer rate of the optical fiber sensor changes dramatically. In general, it drops rapidly as the strain in the host matrix increases and along the axis towards the end of the sensor. Figure 5.8 shows the spatial distribution of the strain transfer rate at various strain levels or plastic damage grades (monolithic function of the strain of the host material as illustrated in figure 5.6). The strain transfer rate significantly varies along the longitudinal direction of the sensor. The highest strain transfer rate is located in the mid-point of the sensor and the strain transfer rate decreases significantly as it approaches to the end. The plastic damage in the host matrix affects the sensor's strain transfer rate. If the plastic damage rises to a point when the strain is larger than 0.21%, the strain transfer rate in the mid-point of sensor drops below 90%. Figure 5.9, a plotted line graph, shows that at various sensor locations, the strain transfer rate decreases at a similar rate as the plastic damage increases. However, because the strain transfer rate at the end of the sensor is much lower than that in the middle range, it is almost below 80%.

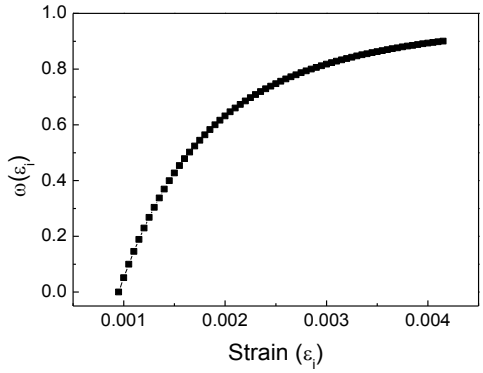

Figure 5.6 Plastic damage function as a function of strain in the host matrix

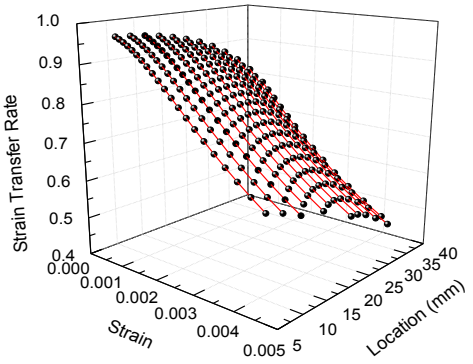

Figure 5.7 Three-dimensional view of strain transfer rate as a function of strain and location

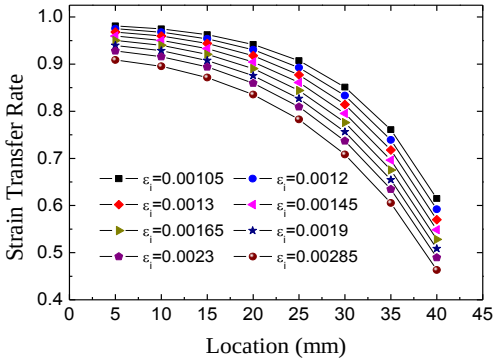

Figure 5.8 Spatial distribution of the strain transfer coefficient at various plastic deformation levels

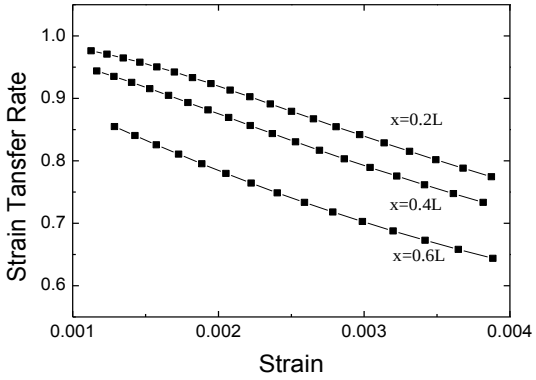

Figure 5.9 Change in strain transfer coefficient with strain levels at various locations

5.1.3 Sensor Design Guidelines Based on the Strain Transfer Theory

Once the plastic damage in the host matrix is determined, the measurement error introduced by the optical fiber sensor can then be calculated as

$$w = 1 - \eta = \frac{\cosh\left(\beta_{ap1} x\right)}{\cosh\left(\beta_{ap1} l_f\right)}. \tag{5.19}$$

The average measurement error $\bar{w}$ can be evaluated by first integrating equation (5.19) from x=0 to x=l_f and then dividing the integration by the length l_f. That is,

$$\bar{w} = \left(l_f \beta_{ap1}\right)^{-1} \tanh\left(l_f \beta_{ap1}\right) \tag{5.20}$$

Let $y = \beta_{ap1} l_f$. The function $\tanh y$ increases with y as shown in figure 5.10. If y is larger than 2, $\tanh y$ is larger than 0.95. If y is larger than 5.3, $\tanh y$ is approximately equal to 1. Therefore, for large y values, equation (5.20) can be approximated by

$$\bar{w} = \left(l_f \beta_{ap1}\right)^{-1} \tag{5.21}$$

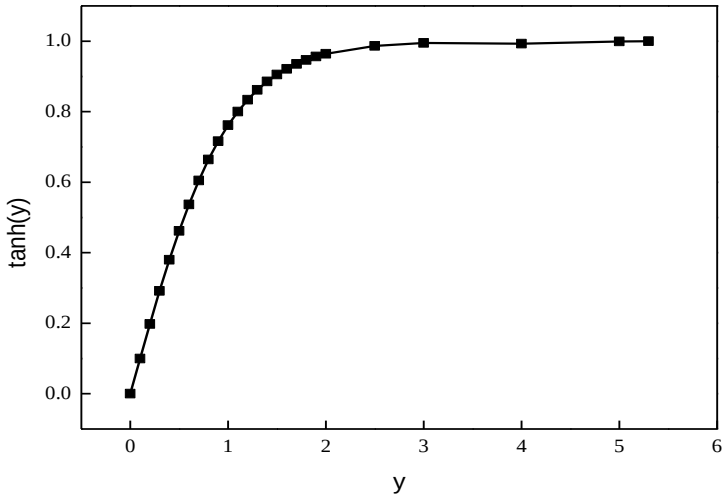

Figure 5.10 Relationship between tanh(y) and y

For an acceptable error in strain measurement w_2, the packaged optical fiber can be designed by the following inequality constraint after equation (5.14) has been introduced for β_{ap1}:

$$\frac{4E_h r_{ap}\left[1 - w(\varepsilon_i)\right]}{3{l_f}^2 E_{ap}\left(r_h - r_{ap}\right)} \le {w_2}^2 . \tag{5.22}$$

Given the material properties of both the host matrix and the packaging layer as well as the sensor length, the radius of the packaged optical fiber sensor can be estimated from:

$$r_{ap} \le \frac{\frac{3E_{ap}{l_f}^2 w_2^2}{4E_h\left[1-w(\varepsilon_i)\right]}}{1+\frac{3E_{ap}{l_f}^2 w_2^2}{4E_h\left[1-w(\varepsilon_i)\right]}} r_h . \tag{5.23}$$

As an example, assume that $\bar{w} \le 5\%$, $E_h = 30Gpa$, $r_h = 25mm$, $l_f = 10mm$, and E_{ap} = 12 GPa. In this case, the maximum radii of the optical fiber sensor that can tolerate various levels of damage in the host matrix are presented in table 5.1. Note that for all cases in table 5.1, y is equal to or larger than 2.0, verifying the validity of $\tanh y > 0.95$.

Table 5.13 Proper sensor radius with various grades of plastic damage

$w(\varepsilon_i)$	0.2	0.3	0.4	0.5	0.6	0.7	0.8
Max. r_{ap} (mm)	2.1	2.4	2.8	3.3	4.0	5.0	6.8
y	4.6	4.1	3.6	3.1	2.6	2.2	2.0

Similarly, given the material properties of the host and packaging materials as well as the radius of the packaged optical fiber, the minimum length of the packaged sensor can be estimated by:

$$l_f \ge \sqrt{\frac{4E_h\left[1-w(\varepsilon_i)\right]r_{ap}}{3E_{ap}w_2^2\left(r_h - r_{ap}\right)}} \tag{5.24}$$

When $\bar{w} \le 5\%$, $E_h = 30Gpa$, $r_h = 25mm$, $r_{ap} = 2.5mm$, and E_{ap} = 12 GPa, the minimum lengths of the optical fiber sensor that can withstand various levels of damage in the host matrix are listed in table 5.2. Note that for all cases in table 5.2, y exceeds 2.0, which verifies the

validity of tanh $y > 0.95$.

Table 5.2 Proper sensor radius with various grades of plastic damage

$w(\varepsilon_i)$	0.2	0.3	0.4	0.5	0.6	0.7	0.8
Min. l_f (mm)	10.89	10.18	9.43	8.61	7.70	6.67	4.40
y (mm)	7.45	6.5	5.6	4.7	3.7	2.8	2.5

5.1.4 A Practical Design Example

This example considers an optical fiber sensor packaged in a coating material of rectangular cross section and attached to a host material (Li, 2005). Between the coated fiber (h_p thick) and the host material is an adhesive layer (h_a=h_0 thick) that is used to transfer strain from the host material to the optical fiber based on the shear lag effect. The strain transfer rate (STR < 1.0) is defined as the strain ratio between the fiber and the host material. For a general multilayer system as an extension of figure 5.5, the strain transfer rate can be derived as follows (Li, 2005):

$$STR = \frac{\bar{\varepsilon}_c}{\bar{\varepsilon}_h} = 1 - \frac{\cosh(\beta l_f) - 1}{\beta l_f \sinh(\beta l_f)} \quad \text{and} \quad \frac{1}{\beta^2} = E_c h_0 [\frac{(3h_0 - 2r_c)(h_0 + 2r_c)}{8 h_0 G_c} + \sum_{i=1}^{n} \frac{h_i}{G_i}] \tag{5.25}$$

where $\bar{\varepsilon}_c$ and $\bar{\varepsilon}_h$ are the average strains of the optical fiber and the host material, respectively; l_f is the attachment length of the optical fiber; β is an eigenvalue related to the adhesive layers as given in equation (5.6); E_c and G_c are the Young's modulus and shear modulus of the optical fiber, and G_i is the shear modulus of the i^{th} adhesive layer of h_i thick.

A specially designed adhesive layer can be introduced to transfer strain from the host structure to the sensor as shown in figure 5.11, thus reducing the strain transfer. The length, width, and thickness of the adhesive layer can be designed based on the required strain range prior to a sensor installation. An experiment was designed with three attachment schemes of the

OF sensors as illustrated in figure 5.11. OF1 was installed at the center points of two adhesive blocks; OF2 and OF3 were attached to two inner and outer points of the adhesive blocks, respectively. As shown in figure 5.11, the host structure was a tapered steel beam (¾ in. thick, 12 in. long and 5 in. wide at the large end) that was cantilevered and subjected to a uniform strain under a concentrated load at its tip.

Figure 5.11 Sensor attachment schemes

For all three cases, table 5.3 summarizes the strain sensitivities of the LPFG sensors with various attachment schemes. In comparison with the calibration sensitivity (+0.00401nm/με), the strain sensitivity (+0.00325 nm/με) remained high through multi-layer adhesives for the sensor attached at the center of adhesives. When attached at two inner points, the tension effect on the optical fiber increased so that the strain sensitivity (negative) lost almost half of its corresponding calibration sensitivity. The opposite case was also true so that the strain sensitivity increased more than twice its corresponding calibration sensitivity. In addition, the multilayer adhesives not only changed the strain sensitivity of the OF sensor but also reduced the bending effect on the OF sensor. Therefore, for large-strain optical fiber sensors, multilayer adhesives of a certain length are a promising mechanism for civil engineering applications.

Table 5.3 Sensing properties of LPFG sensors with multilayer adhesives for strain transfer

Sensor designation	Support location	Initial center wavelength (nm)	Strain sensitivity (nm/με)	Calibration sensitivity (nm/με)
OF1	Center	1553.132	+0.00325	+0.00401
OF2	Inner	1547.380	-0.00032	-0.00059
OF3	Outer	1551.855	-0.00148	-0.00059

5.2 Strain Transfer Mechanism Based on Gauge Length Change

The mechanics of materials (Cook, 1999) indicates that the average strain of a tension member is inversely proportional to the gauge length between two observation points. Thus, by introducing a gauge length change mechanism, the strain in an optical fiber sensor attached to a structure can be significantly smaller than that of the structure, achieving a small strain transfer rate. Figure 5.12 shows that two rigid blocks of a host structure move apart, resulting in deformation in OF1 and OF2 sensors. The OF1 measures the strain over a length L representing the structural strain in practical applications, whereas the OF2 sensor measures the strain over a length L+2s. Therefore, the STR can be represented by:

$$STR = \frac{\varepsilon_{LPFG2}}{\varepsilon_{structure}} = \frac{L}{L+2s} \tag{5.26}$$

when the adhesive length *s* is equal to *L/2*, equation (5.26) yields an STR of 0.5.

For example, if the structure was subjected to 3,000 $\mu\varepsilon$, the OF2 would perceive only 1,500 $\mu\varepsilon$ as a result of the reduced deformation of the optical fiber.

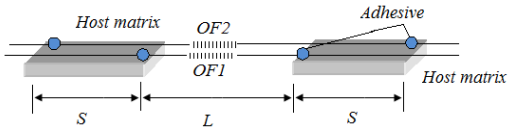

Figure 5.12 Gauge length change mechanism

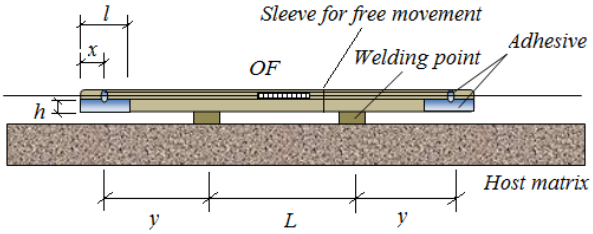

Figure 5.13 OF sensor with a hybrid mechanism

A simple test shown in figure 5.12 was set up to study the feasibility of strain transfer based on gauge length changes. In this case, two sensors (OF1 and OF2) were subjected to axial deformation. Their sensing properties are summarized in table 5.4. The strain sensitivity of OF2 reduced the corresponding calibration value of the strain sensitivity by more than half as the sensing gauge length doubled, verifying the strain transfer mechanism. However, given the difficulty of senor installation and the property requirements, the maximum strain sensitivity adjustment that a gauge length change based OF sensor can achieve is approximately 25% as shown in figure 5.14.

Table 5.4 Sensing properties of optical fiber sensors with gauge length changes

Sensor designation	Initial center wavelength (nm)	Strain sensitivity (nm/με)	Calibration strain sensitivity (nm/με)
OF1	1593.444	-0.000521	-0.00053
OF2	1593.752	-0.000380	-0.00072

5.3 Large-strain Optical Fiber Sensors with a Hybrid Transfer Mechanism

The two basic strain transfer mechanisms discussed in the previous sections can be combined to develop a hybrid transfer mechanism as illustrated in figure 5.13. Such an optical fiber sensor has multilayer adhesives at each end. The fiber is placed inside a stiff structural member, such as a steel tube (which can be welded to the host structure) or a glass tube (which can be attached to the host structure) with adhesives at two points L distance apart. The tube

consists of two parts with a sleeve joint between the two supports on the host structure to facilitate their relative axial elongation. The strain measured with the optical fiber sensor over a length of L+2s is first converted to the strain between the two sensor attachment points on the tube. This strain is in turn converted to the average strain over the length (L). Therefore, the STR of the hybrid mechanism is actually equal to equation (5.25) multiplied by equation (5.26). The steel or glass tube can protect the sensor from damage, environmental disturbance, and bending effect. Figure 5.13 shows a numerical example designed to test the performance of this hybrid strain transfer mechanism. The setup combines the two basic mechanisms described in sections 6.1 and 6.2. Figure 5.14 compares the strain in the optical fiber with that in the host structure for four cases: without strain transfer effect, with shear lag effect, with gauge length change, and with shear lag and gauge length change (hybrid mechanism). The case without strain transfer is the benchmark. Figure 5.14 shows that the slopes corresponding to these three mechanisms (or the STR values) are lower than the slope of the benchmark case. The hybrid mechanism shows the lowest slope, followed by the gauge length change, and finally the shear lag. The calibration sensitivity is the highest without strain transfer. In this example, the effects of shear lag and gauge length change were similar. The effect of the hybrid mechanism is approximately equal to the combined effects of both shear lag and gauge length change. Thus, the optical fiber sensor with the hybrid mechanism can measure the level of strains in structures up to 7,200 με. This level is approximately 2.5 times the breaking strain of the optical fiber sensor itself. Since the sensors based on shear lag and gauge length change are limited to the strain sensitivity adjustments of 50% and 25%, respectively, the maximum strain sensitivity adjustment of the sensor based on the hybrid mechanism is 12.5%. The maximum strain for this sensor is 24,000 με as shown as a line graph in figure 5.14.

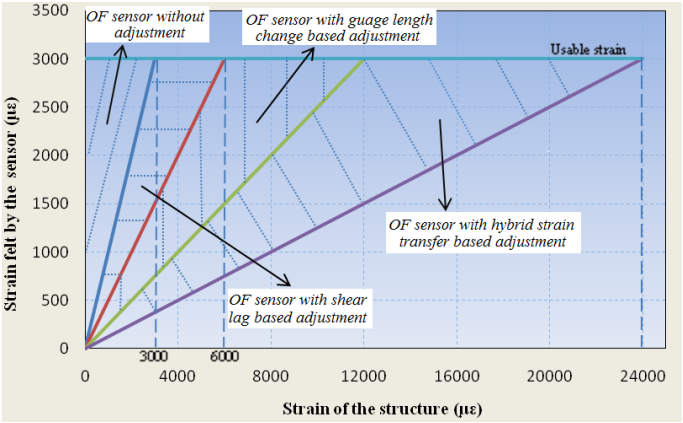

Figure 5.14 Effects of various strain transfer mechanisms

a) Gauge length change (OF1)

b) Hybrid strain transfer (OF2)

Figure 5.15 Sensor structure and test setup

Based on the strain transfer theory, large-strain sensors have been developed and their strain sensitivity and sensing properties evaluated with tensile tests. Figure 5.15(a) shows a photograph of the large-strain sensor based on gauge length change only. The sensor is packaged in a small steel tube (with a gauge length of 10 mm) to ensure that it can move smoothly with the deformation of the host structure. The small steel tube is enclosed in a large steel tube that serves as a sleeve. Figure 5.15(b) shows a photograph of the large-strain sensor based on the hybrid strain transfer. It is also packaged in a small steel tube, which is installed in two larger steel tubes. Parts of the larger steel tubes are cut into half tubes so that the adhesive of the appropriate length and thickness can be inserted into the tube. The sensor is attached to the larger steel tubes at two points (a gauge length of 15 mm apart) on the adhesive blocks (each of which is 3 mm long and 1 mm thick). Both the packaged sensors are installed on an aluminum sheet using adhesives. OF1 sensor has a gauge length of 5 mm, and OF2 sensor has a gauge length of 6 mm.

Table 5.5 summarizes the test results. They indicate that if the strain of the host structure is approximately 16,000 με, the strain in OF1 is approximately 9,000 με and that in OF2 is approximately 6,000 με. The strain transfer rate of OF1 is 61.1%, and that of OF2 is 22.8%, whereas the theoretical strain transfer rates of these sensors are 50% and 28% respectively. Thus,

the experimental and theoretical results are in good agreement. This test verified the applicability of the proposed strain transfer mechanism for the design of large strain sensors.

Table 5.5 Sensing properties of the sensors with gauge length changes for strain transfer

Sensor designation	Initial center wavelength (nm)	Strain sensitivity (nm/με)	Calibration strain sensitivity (nm/με)	Actual strain transfer rate (%)	Theoretical strain transfer rate (%)
OF1	1563.720	-0.000642	-0.00105	61.1	50
OF2	1559.613	-0.000438	-0.00192	22.8	28

5.4 PP-FRP Packaged Large Strain Optical Fiber Sensor Based on Shrinkage

Equation (5.7) indicates that the geometry and the material property of both the host structure and the package layer control the strain transfer effect. However, the high strain transfer rate by gauge length change can significantly correspond to the reduced sensor sensitivity. In addition, the gauge length change mechanism can only be implemented for surface installation.

This section introduces another large strain sensing concept based on the shrinkage of the packaging material during concrete casting so that the optical fiber is actually prestressed prior to external loading. Polypropylene (PP) can shrink significantly during curing, and it has been widely used for fiber reinforcement of polymers. Therefore, PP-FRP-packaged optical fiber sensors can be manufactured for large strain measurement as shown in figure 5.16.

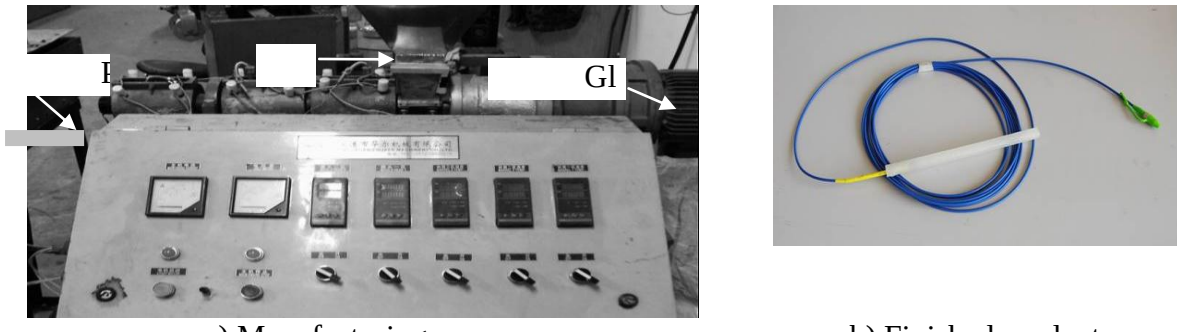

a) Manufacturing process b) Finished product

Figure 5.16 PP-FRP-packaged optical fibers

To demonstrate the shrinkage mechanism for large strain measurement, fiber Bragg

gratings (FBG) were inscribed on an optical fiber that was packaged with a PP-FRP layer. The FBG measurements were taken as the PP materials were being cured. The recorded strains from the FBG sensor are presented as a graph in figure 5.17. It can be clearly observed from figure 5.17 that the level of strains generated due to material shrinkage can be as high as 12,000 με.

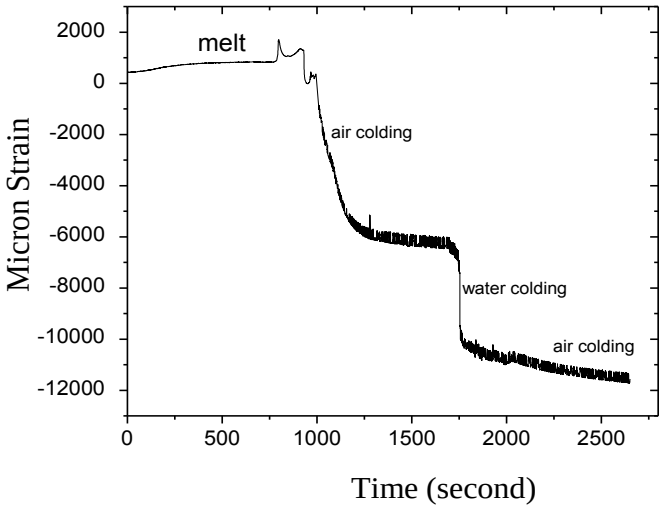

Figure 5.17 Internal strain change during manufacturing of a PP-FRP-packaged optical fiber

To further understand the sensor property in applications, the FBG sensor installed in the PP-FRP layer during protruding was characterized under tensile tests. Figures 5.18 and 5.19 show the test setup and the tensile test data in plotted line graphs. The test results indicate that the PP-FRP -packaged FBG sensor prestressed to -12,000 $\mu\varepsilon$ has a sensing coefficient of 0.85 pm/$\mu\varepsilon$, which is quite sensitive compared with FBG sensors without prestressing and stable under cyclic loading. In this case, if the breakage strain of an FBG optical fiber sensor is about 30,000 $\mu\varepsilon$ under no prestressing, the ultimate strain of the FBG with prestressing can be as high as 42,000 $\mu\varepsilon$. In addition, such a coated sensor can be easily embedded in concrete structures due to their ruggedness.

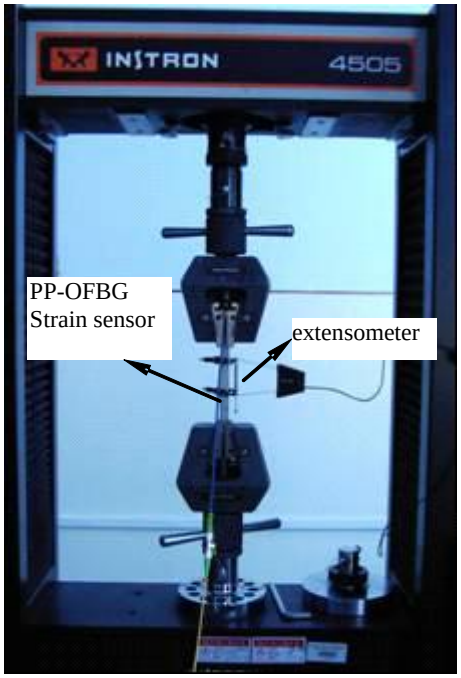

Figure 5.18 Test setup of a PP-FRP-packaged optical fiber sensor

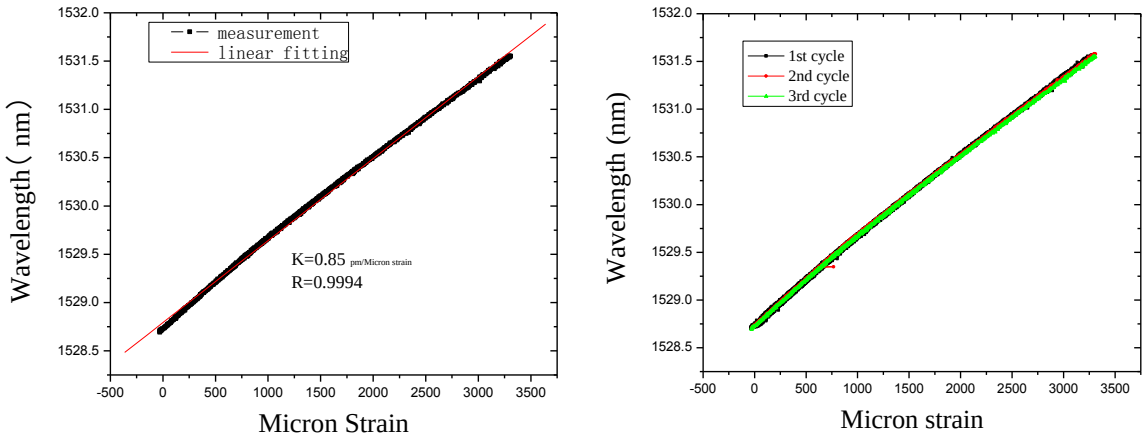

a) Strain sensing coefficient b) Robustness test under cyclic loading

Figure 5.19 Sensor properties of PP-FRP-packaged optical fibers

Chapter 6 Implementation of Rugged Optical Fiber Sensors for Large Strain Measurements

6.1 RC Beam Monitoring Using Distributed Optical Fiber Sensors

In this section, the BOTDA-FBG collinear technique was applied to measure strains in a RC beam of 2700 mm × 200 mm × 400 mm. Figure 6.1 illustrates the experimental setup of the beam under four point loading in a diagram. As shown in the photographs in figure 6.2, a surface-attached FRP-FBG strain sensor and an FRP-optical fiber (FRP-OF) strain sensor were installed on the bottom surface of the RC beam. One bare OF and one electrical resistance strain gauge (ERS) were also attached on bottom surface of the RC beam for comparison. The two FRP-coated OF sensors and the bare OF were placed in parallel, and the ERS was located in the mid-span of the RC beam. For the convenience of signal interrogation, the initial wavelength of the FBG was set to be about 1565 nm, which is far away from 1550 nm that represents the characteristic wavelength of the BOTDR system.

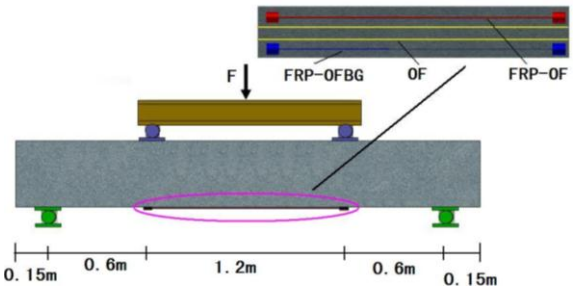

Figure 6.1 Schematic of the test setup of an RC beam under four-point loading

a) Sensor attachment

Figure 6.2 Sensor attachment and test setup

Each beam was loaded with a hydraulic actuator in an incremental step of 6 kN and then held for 5 min while taking strain measurements. Figure 6.3 presents the mid-span strains measured by various sensors. It can be seen from figure 6.3 that the strains measured by the FRP-FBG sensor are in good agreement with those by the BOTDA with the FRP-OF, the BOTDA with the bare OF, and the reference ERS sensors both at loading and unloading cycles. The maximum relative difference in strain measurement by the FRP-FBG sensor and BOTDA with the FRP-OF sensor was approximately 6% except at small loads. This comparison verified the accuracy of strain measurements with both the point FBG sensor and the distributed BOTDA sensor.

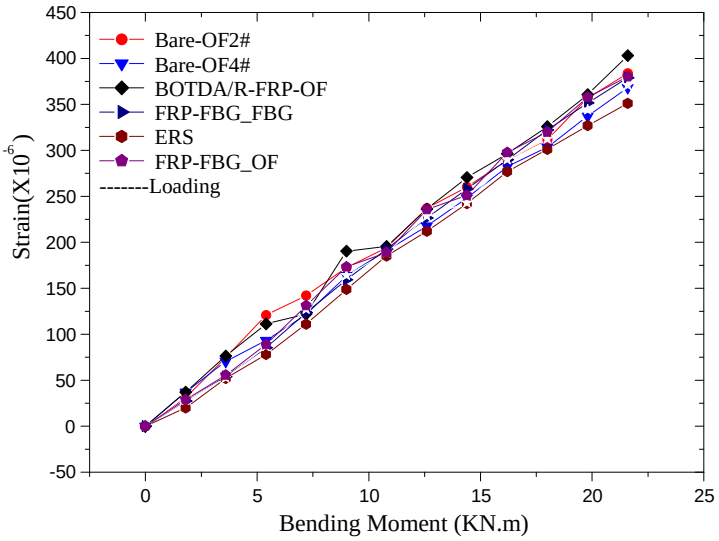

a) Loading cycle

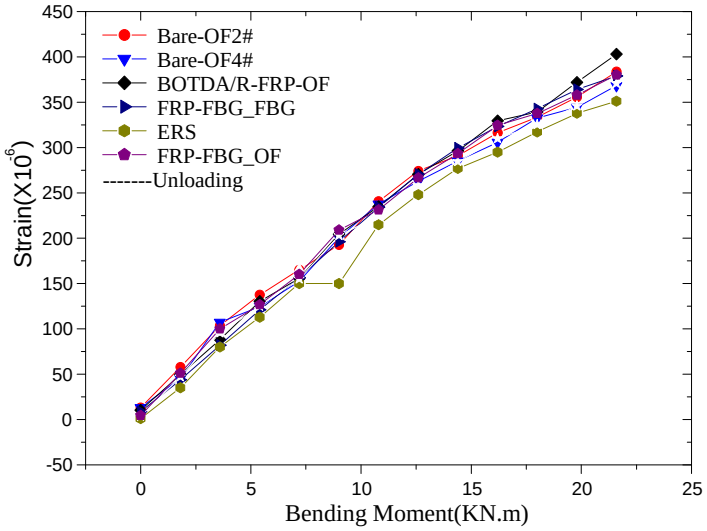

b) Unloading cycle

Figure 6.3 Strains in RC beam at load and unload cycles

Figure 6.4 shows the strain distribution of the BOTDA measurements with the FRP-FBG OF. The mid-span strain measured by the BOTDA system agrees well with that measured at the same point by the FBG system. Figure 6.5 compares the strain measurements taken at the mid-span of the RC beam at increasing loads. All the strain curves had a kink point at approximately 45 kN when a few cracks of as wide as about 0.3 mm were visually observed at

the bottom side and mid-span of the RC beam. As the applied load was continually increased, the cracks expanded and the strain curves from different sensors began to diverge. When the load reached about 160 kN, the anchor of the FRP-FBG OF began to slip from the concrete surface, rapidly relieving the strain. The test results indicate that the collinear FRP-FBG and BOTDR sensors can effectively measure the mid-span strain of the RC beam at various load levels, compared to other sensors including the conventional ERS.

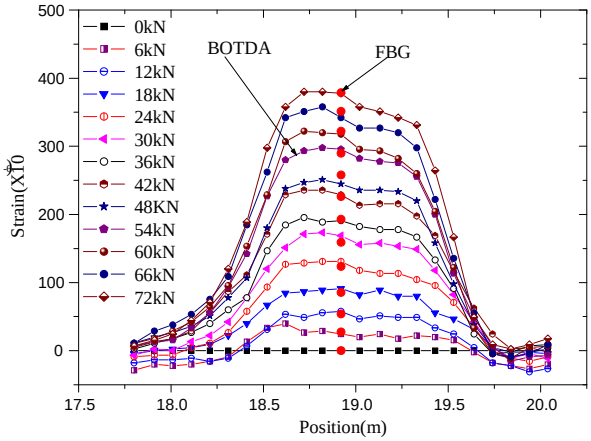

Figure 6.4 Strain measurements by the BOTDA and FBG sensors

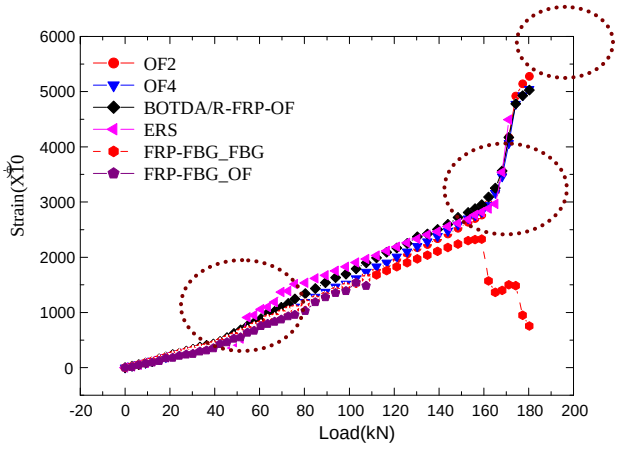

Figure 6.5 Mid-span strain measurements by various sensors

6.2 A Smart Cable with Embedded Optical Fiber Sensor

The key load-bearing components of a cable-stayed bridge are stay cables, which transfer

most of the loads from the bridge deck to the bridge towers and then the bridge foundation. The stay cables are distributed along the length of the bridge with large span lengths. They often serve in harsh environments and are vulnerable to random damage. To ensure the safety of a cable-stayed bridge, it is critically important to monitor the loading condition of the stay cables.

This section proposes a new cable monitoring method with FBG and BOTDA measurements using a single optical fiber (Zhou and Chen, 2009). This method can accurately measure the local force at critical points and monitor the distributed loading information along the full length of a stay cable. The fabrication procedure, the measurement principle, and the sensing property of the new monitoring method that are discussed have been tested and validated with a series of experiments as discussed below.

To add the sensing capability to a stay cable, FRP-OF rebar, FRP-FBG rebar, or collinear FRP-OF-FBG rebar was integrated into a stay cable during the fabrication process. As shown in figure 36, two or three FRP-FBG rebar were symmetrically deployed over the cross section of the stay cable so that the potential cable force measurement error due to decentering of the cable or the applied load could be eliminated and additional redundancies were introduced. Figure 6.7 shows the fabrication procedure for a smart FRP-OF/FBG stay cable. First, two FRP-FBG rebar with cable wires of equal length were symmetrically laid out along with the cable wires and then protected by polyethylene (PE) materials, as shown in figures 37(b) and 37(c). Second, the two FRP-FBG rebar were placed in series and fusion-spliced together for easy measurement with one instrument in practical applications. The splicing point of the two optical fibers was protected by a brass tube as shown in figure 6.7(d). Finally, a mixture of epoxy and iron beads was infused into the anchor and solidified by heating, as shown in figures 6.7(e) and 6.7(f).

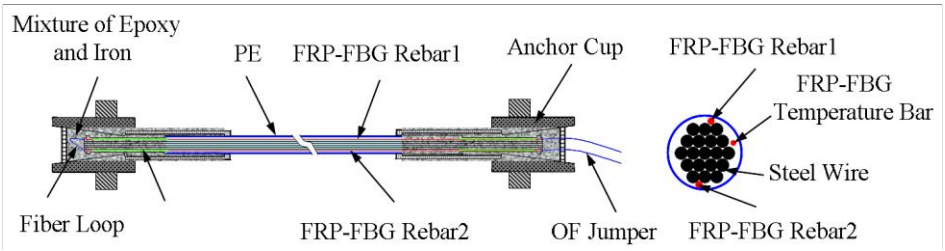

Figure 6.6 A smart FRP-FBG stay cable

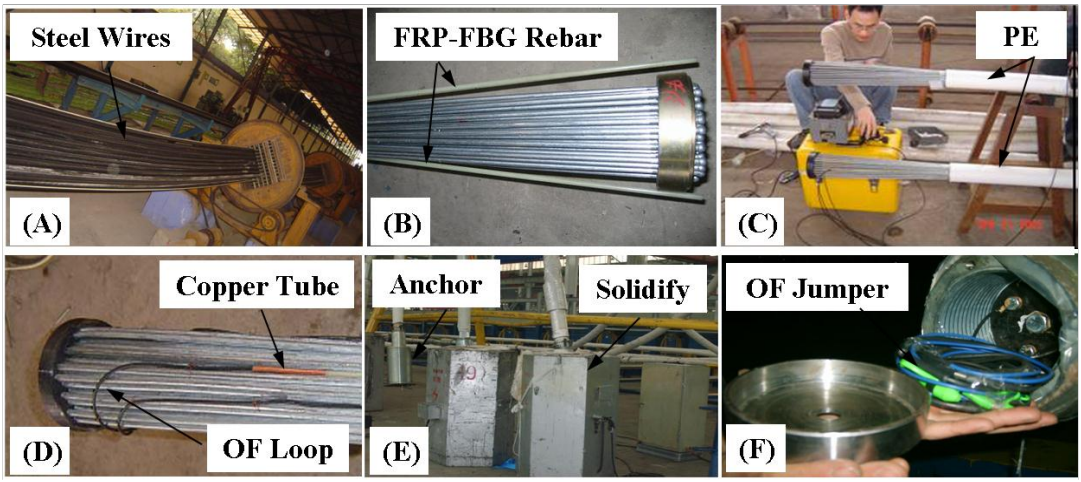

Figure 6.7 Fabrication process of a smart stay cable

The FRP-FBG or FRP-OF rebar was made by embedding one or more FBGs or optical fibers into an FRP rebar for improved ruggedness, durability, and fatigue resistance. The optical fibers were coated with polyimide to survive temperatures up to 250°C over a long period of time. The embedded FBGs were chosen to have resonance wavelengths separated by at least 2~3 nm so that they can be interrogated simultaneously by an FBG interrogator (SI720 by Micron Optics, Inc.). In addition, the gap between the hole on the anchor plate and the fiber jumper was small enough to prevent the epoxy from leaking into the fiber jumper and making the optical fiber more fragile. For field deployments, one FRP-FBG or FRP-OF rebar with a small diameter (~3 mm) was also installed along with the strain sensing rebar. To isolate it from external loading, however, the small FRP-coated FBG sensor or OF was contained in a stainless steel

pipe, which acted as a temperature compensation sensor. Two smart cables were selected to verify the sensing properties of embedded FBG sensors. Table 6.1 lists the specifications of the two cables designated as C1 and C2 based on their initial FBG wavelengths.

Table 6.1 Stay cable specifications

Cable	Initial FBG wavelength (nm)	Length of cable (m)	Number of steel wires	Cable force sensitivity coefficient (nm/kN)
C1	1555,1560	15.384	109	1.36×10^{-3}
C2	1525,1530	30.842	61	2.43×10^{-3}

The calibration tests of the stay cables were conducted on a horizontal tensile machine with a 1000 T load capability, as shown in figure 6.8. The integrated optical measurement system consisted of an FBG interrogator, a BOTDA instrument, and an optical switch or coupler. The FBG interrogator, made by Micron Optics Inc. (SI720), recorded the resonance wavelength of the embedded FBG sensors. The strain measured by the Brillouin optical fiber sensors was recorded by DiTeSt STA200 produced by Omnisens in Switzerland with a spatial resolution of 0.5 m and a measurement accuracy of $\pm 20\mu\varepsilon$.

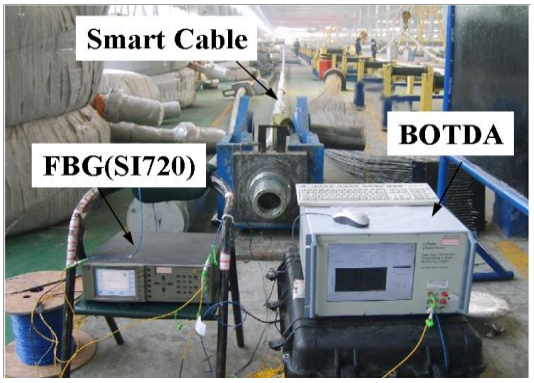

Figure 6.8 Test setup and measurement systems

Figure 6.9(a) presents the Brillouin frequency shift (BFS) distribution along the FRP-OF-FBG rebar. The first half of the Brillouin signal denotes the first rebar, and the second denotes the second rebar. Figure 6.9(b) shows the strain distribution along the cable by averaging the measurements of the two FRP-OF-FBG rebar. The test results indicate that under an axial load, the strain varied along the length of a stay cable due to different twist angles and varying cross sectional areas of steel wires as well as inconsistency contact strengths between the FRP rebar and the steel wires. The cable forces measured at the anchorage and tension ends were larger than those measured at the mid-point of the cable. This difference can be attributed to the stress concentration due to the Saint-Venant effect. Under the same applied load, the cable strain measured in the loading (L) cycle was smaller than that in the unloading (U) cycle. This hysteresis was largely due to the friction between the tension equipment and the tension desk.

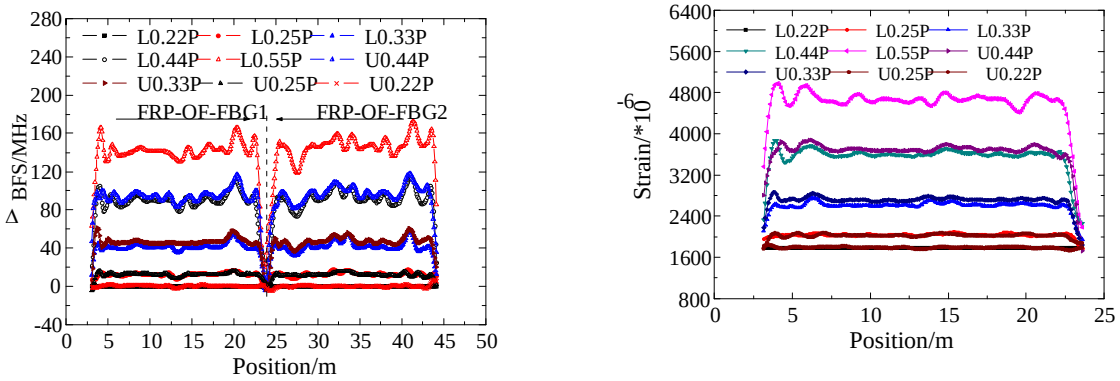

a) Brillouin frequency shift distribution b) Average strain distribution of cable

Figure 6.9 Strain measurements by BOTDA

6.3 A Smart Steel Strand with Embedded Optical Fiber Sensor

Prestress loss adversely affects the behavior of in-service post-tensioned structures in terms of deflection or camber, cracking, and ultimate capacity. It is thus important to determine the level of prestress at various loading stages from the initial prestress transfer to the structure,

through various in-service loads, to the ultimate load of the structure. Prestress loss is difficult to evaluate due to several related factors such as creep, shrinkage, relaxation, geometric configuration, distributed friction, and slippage of post-tensioned strands. This section develops a novel smart FRP-FBG or FRP-OF steel strand by replacing the middle steel wire with FRP-FBG-OF or collinear FRP-OF-FBG rebar in a seven-wire prestressed steel strand for long-term monitoring of prestress loss.

Figure 6.10 shows the schematics and cross section of a smart FRP-FBG-OF steel strand. It consists of a smart FRP rebar and six 5-mm-diameter steel wires surrounding the rebar. To ensure effective bonding between the FRP rebar and the wires, the FRP rebar was wrapped in a high-ductility copper sheet. Since the FRP rebar is deformed together with the remaining six steel wires, the deformation of the steel strand can be measured directly by the optical fiber sensor embedded in the FRP rebar. In practical applications, smart steel strands can be installed on bridges in the same way as traditional strands, and will therefore be easy to implement after the technology has been thoroughly validated.

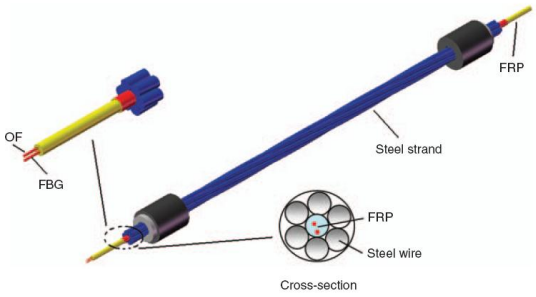

Figure 6.10 Schematic view and cross section of a smart FRP-FBG-OF steel strand

The sensing properties of a smart steel strand were validated with a tension test as illustrated by the photographs in figure 6.11(a) for BOTDA measurements and in figure 6.11(b) for measurements by an FBG sensor installed at the middle of the optical fiber.

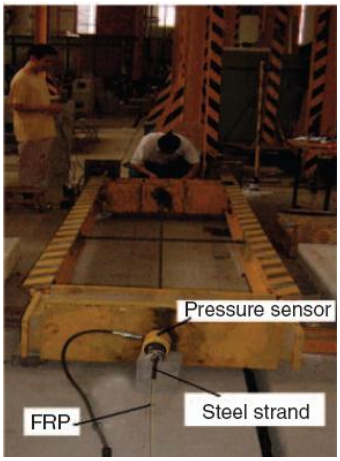

a) BOTDA distributed sensing b) FBG point sensing

Figure 6.11 Setup for validation test of a smart steel strand

Figures 6.12(a) and 6.12(b) present the strain distributions obtained from the BOTDA system under an axial load, and the point strains measured by the FBG sensing system as a function of the applied load. The applied load was measured by a pressure sensor and converted to the strain applied to the steel strand. With a calibration curve of the FBG sensor, the directly measured wavelength can be converted into the measured strain. The BOTDA/R can measure the distributed strain along the steel strand. In particular, the slippage at certain fixed points, which is crucial for structural safety evaluation, can be inferred from the distributed strain measurements. The data taken from the two optical fiber systems can be verified against each other or used to compensate for temperature effects when the temperature along the steel strand is nearly constant. As shown as multiple line graphs in figure 6.12(a), the strain varies along the cable length since the steel strand in a prestressed structure is subjected to external loads at points of contact, such as the interfaces with concrete, ducts, anchoring, and dead weights. As shown in figure 6.12(b), the coefficients of determination (R^2) between a linear regression line and the test data from the FBG sensor are over 0.9995. This result indicates that the measured strain is linearly related to the applied load.

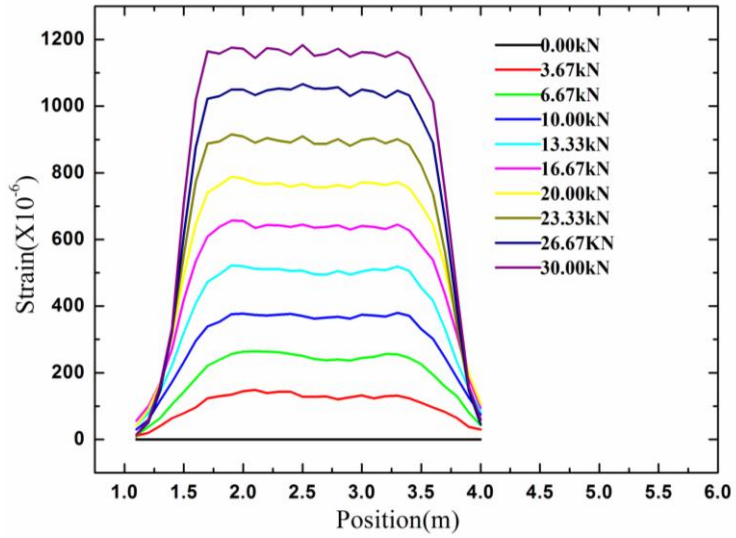

a) BOTDA distributed sensing

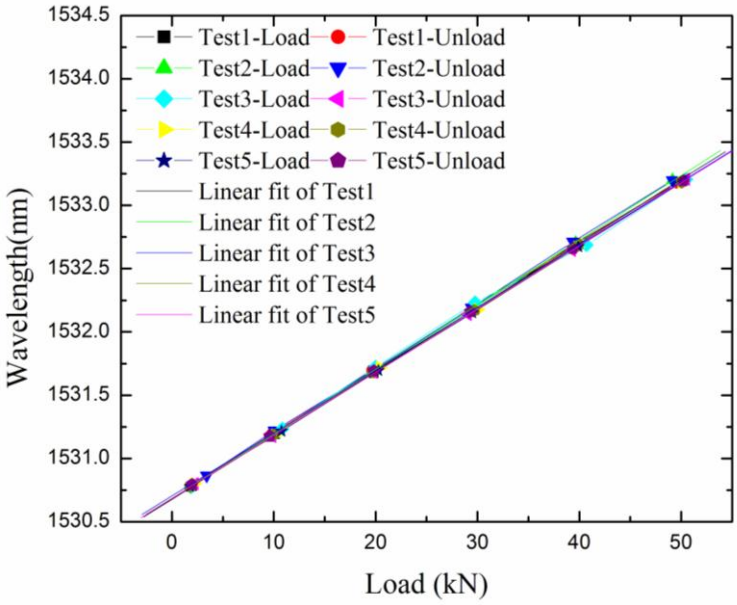

b) FBG point sensing

Figure 6.12 Experimental results of a smart steel strand

Chapter 7 Research Findings and Recommendations

Based on the extensive experiments and analysis in this study, the main research findings and recommendations are summarized below.

7.1 Ruggedness Characterization and Performance Comparison among Various Packaged Optical Fibers

Among all the optical fibers tested in this study, SMF-28 optical fibers with uncoated anchoring have the lowest shear strength and the lowest ultimate strain under tension, and are thus not suitable to apply in harsh environments. Polyimide-coated optical fibers have the highest shear strength and the highest ultimate strain under tension, making them the best candidate for civil infrastructure applications. GFRP-coated optical fibers have relatively high shear strength, but can withstand the largest shear force since they can be fabricated with a significantly large diameter. Carbon-coated optical fibers also have relatively high shear strength and a large ultimate strain under tension. Both GFRP- and carbon-coated optical fibers are sufficiently rugged to be applied to civil infrastructure as well.

The strain sensing coefficients of all the coated optical fibers using a BOTDR/A distributed strain sensing system are similar to those of bare optical fibers. Therefore, the use of elastic coatings for optical fibers to improve the fiber ruggedness will not necessarily compromise the sensing properties of the fibers.

All the coated optical fibers show satisfactory corrosion resistances in 20% NaCl solution since optical fibers are made of glass (silica) that are typically durable in acid solutions. However, further tests are needed to characterize the corrosion performance of optical fibers in alkali solutions such as the concrete pore solution in RC structures since the high alkaline environment may directly attack glass, causing optical fiber degradation.

7.2 Large-strain Sensor Development

Strain transfer with material elasticity is an effective design strategy for large strain

measurement using optical fiber sensors. This mechanism not only provides a large degree of flexibility in large-strain sensor design, but also preserves the strain sensitivity of optical fiber sensors. The strain transfer theory developed in this study can be used to guide a practical design of large-strain optical fiber sensors. The use of a multi-layer strain transfer system may make a packaged optical fiber become bulky in practical applications.

Strain can be simply defined as the deformation over a base length. Therefore, increasing the so-called gauge length of an optical fiber strain sensor allows the measurement of larger deformation by the sensor. Gauge length change is thus an effective way to modify the strain applied to an optical fiber. However, this method may compromise the strain sensitivity of the optical fiber sensor since the measured strain represents the average deformation over the gauge length. As a result, this mechanism for the reduction of ultimate strain applied on optical fibers may be limited in practical applications. In addition, a gauge length change scheme is more practical in a surface attachment instead of an internal embedment of concrete structures.

Polypropylene significantly shrinks in its curing process. It can be used to coat an optical fiber so that, when cured, it compresses the fiber with a prestressing force. Indeed, one example indicated that a compressive strain of as high as 12,000 με can be achieved with this mechanism. Therefore, prestressing with material shrinkage properties is an effective way to make large-strain measurements with low-module optical fiber sensors.

A hybrid mechanism of reducing the strain applied on optical fibers can be very practical and effective for civil infrastructure applications. The hybrid mechanism can combine the strain transfer with material elasticity and the gauge length change for surface attachment applications or the strain transfer and the prestressing with material shrinkage for internal embedment applications. It is recommended that a hybrid strain reduction mechanism be considered in practical designs of large-strain measurements.

7.3 Application of Rugged Optical Fiber Sensors for Large-strain Measurements

As validated by commercial strain gauges, both FBG and BOTDR/A optical fiber sensors can be used to accurately measure strains in civil infrastructures. Their recorded signals can be interrogated without difficulty.

A single optical fiber with an FBG sensor can be used for both a point strain measurement at the location of the FBG and a distributed strain measurement along the length of the fiber using a BOTDR/A system. The two interrogation schemes can be combined to determine strain and temperature simultaneously provided the temperature variation around the FBG is very low. FRP-coated optical fibers can be easily integrated into various key structural components for large strain or stress measurements, such as smart cables and smart strands.

A distribution monitoring technique based on coated optical fibers is highly desirable for the investigation of strain or crack distributions in large-scale concrete structures in civil engineering.

References

Afshar V, S., L. Chen, and X. Bao. 2005. "CW Pre-injection of Pump-probe Brillouin Sensors for High Spatial and Strain (Temperature) Resolutions." *Proc. of SPIE* 5855:5767.

Bao, X., D. J. Webb, and D. A. Jackson. 1994b. "Combined Distributed Temperature and Strain Sensor Based on Brillouin Loss in an Optical Fiber." *Optics Letters* 19:141-143.

Bao, X., D. J. Webb, and D. A. Jackson. 1993. "Characteristics of Brillouin Gain Based Distributed Temperature Sensors." *Electronics Letters* 29.17:1543-4.

Bao, X., D. J. Webb, and D. A. Jackson. 1994. "Recent Progress in Experiments on a Brillouin Loss-based Distributed Sensor." *SPIE - Int Soc Optical Engineering* 20372:506-9.

Bao, X., J. Smith, and A. Brown. 2002. "Temperature and Strain Measurements Using the Power, Line-width, Shape, and Frequency Shift of the Brillouin Loss Spectrum." *Proc. of SPIE* 4920:311.

Bao, X., L. Zou, Q. Yu, and L. Chen. 2004. "Development and Applications of the Distributed Temperature and Strain Sensors Based on Brillouin Scattering." *IEEE Journal* 4:1210-1213.

Bastianini, F., M. Cargnelutti, A. Di Tommaso, and M. Toffanin. 2003. "Distributed Brillouin Fiber Optic Strain Monitoring Applications in Advanced Composite Materials." *Proceedings of the 10th SPIE Annual Symposium on Smart Structures and Materials*, 5057:478-485.

Bastianini, F., A. Rizzo, N. galati, U. Deza, and A. Nanni. 2005. "Discontinuous Brillouin Strain Monitoring of Small Concrete Bridges Comparison between Near-to-surface and Smart FRP Fiber Installation Techniques." *Proc. of SPIE* 5765:612.

Brown, K., A. W. Brown, and B. G. Colpitts. 2006. "Combined Raman and Brillouin Scattering Sensor for Simultaneous High-resolution Measurement of Temperature and Strain." *Proc. of SPIE* 6167:309-318.

Chen, G., B. Xu, R. McDaniel, X. Ying, D. Pommerenke, and Z. Wu. 2005. "Distributed Strain Measurement of a Large-scale Reinforced Concrete Beam-column Assembly under Cyclic Loading", *Proc. of SPIE* 5765:516.

Culverhouse, D., F. Farahi, C. N. Pannell, and D. A. Jackson. 1989. "Potential of Stimulated Brillouin Scattering as Sensing Mechanism for Distributed Temperature Sensors." *Electronics Letters* 25.14:913-915.

Davis, M. A., A. D. Kersey. 1996. "Separating the Temperature and Strain Effects on Fiber Bragg Grating Sensors Using Stimulated Brillouin Scattering." *Proc. of SPIE* 2718:270-278.

DeMerchant, M. D., A. W. Brown, X. Bao, and T. W. Bremner. 1998. "Automated System or Distributed Sensing." *Proc. of SPIE* 3330:315.

Ding, Y., B. Shi, Y. Sun, and Y. Zhao. 2006. "Monitoring on the Arch Rings Deformation in the NO.3 Tunnel of Bainijing with BOTDR Based Strain Measurement Technique." *Journal of Engineering Geology* 15.4:649-653.

Fellay, A., L. Thévenaz, M. Facchini, M. Nikles, and P. Robert. 1997. "Distributed Sensing Using Stimulated Brillouin Scattering : towards Ultimate Resolution." *OSA Technical Digest Series* 16:324-327.

He, J. P., Z. Zhou, Y. Huang, and J. Ou. 2008. "Study on RC Beams Using BOTDA(R)-FRP-OF Technique." *Proc. of SPIE* 6933:69330U-7.

He, Y. J., C. Q. Yin, Y. Q. Li, and Z. Zhang. 2004. "A Novel BOTDR System Based on all Fiber Mach-Zehnder Interferometer." *Act Photonica Sinica* 33.6:721-724.

Horiguchi, T. K. Shimizu, T. Kurshima, and Y. Koyamada. 1995. "Advances in Distributed Sensing Techniques Using Brillouin Scattering." *Proc. of SPIE* 2507:126-135.

Horiguchi, T., T. Kurashima, and M. A. Tateda. 1990. "A Technique to Measure Distributed Strain in Optical Fibers." *IEEE Photonics technology Letters* 2.5:352-354.

Horiguchi, T., T. Kurashima, and M. A. Tateda. 1989. "Tensile Strain Dependence of Brillouin Frequency Shift in Silica Optical Fibers." *IEEE Photonics technology Letters* 1.5:107-108.

Inaudi, D. and B. Glisic. 2006. "Integration of Distributed Strain and Temperature Sensors in Composite Coiled Tubing." *Proc. of SPIE* 6167:17.

Inaudi, D. and B. Glisic. 2006. "Reliability and Field Testing of Distributed Strain and Temperature Sensors." *Proc. of SPIE* 6167:6167D.

Inaudi, D. and B. Glisic. 2005. "Development of Distributed Strain and Temperature Sensing Cables." *Proc. of SPIE* 5855:222-225.

Kato, S. and H. Kohashi. 2006. "Study on the Monitoring System of Slope Failure Using Optical Fiber Sensors." *Proc. of ASCE* 187.34:1-6.

Kee, H. H., G. P. Lees, and T. P. Newson. 2000. "Spontaneous Brillouin-based Distributed Temperature Fiber Sensor with 35-cm Spatial Resolution." *Proc. of SPIE* 4074:237-244.

Kinzo, K., C. H. Li, and K. Nishiguchi. 2005. "Pulse Pre-pump Method for cm-order Spatial Resolution of BOTDA." Proc. of SPIE 5855:559-562.

Kurashima, T., T. Horiguchi, H. Izumita, S. Furukawa, and Y. Koyamada. 1993. "Brillouin Optical-fiber Time Domain Reflectometry." IEICE TRANSACTIONS on Communications E76-B.4:382-390.

Kurashima, T., T. Horiguchi, H. Ohno, and H. Izumita. 1998. "Strain and Temperature Characteristics of Brillouin Spectra in Optical Fibers for Distributed Sensing Techniques." *Proc. of ECOC''98*, 1:149-150.

Kwon, I. B., C. Y. Kim and M. Y. Choi. 2002. "Continuous Measurement of Temperature Distributed on a Building Construction." *Proc. of SPIE* 4696:273-283.

Liang, C., B. Shi, and H. Xu. 2004. "BOTDR Optical Fiber Temperature Monitoring Technique and Its Application in Civil Engineering." *Journal of Disaster Prevention and Mitigation Engineering* 24.3:252-235.

Liu, D. and M. Song. 2005. "A Novel BOTDA Technique Based on Continuous Lightwave Pump." *Optical Instruments* 27.3:1.

Liu, J., B. Shi, D. Zhang, H. Sui, and W. Suo. 2006. "Experimental Study of Foundation Pit Monitoring Using BOTDR-based on Distributed Optical Fiber Sensor." *Rock and Soil Mechanics* 27.7:1225-1233.

Mizuno, Y., Z. He, and K. Hotate. 2008. "Brillouin Optical Correlation-Domain Reflectometry with 13-mm Spatial Resolution and 50-Hz Sampling Rate." *Proc. of Lasers and Electro-Optics CLEO*:CMZ2.

Mohamad, H., P. J. Bennett, K. Soga, R. J. Mair, C. S. Lim, C. K. Knight-Hassell, and C. N. Ow. 2007. "Monitoring Tunnel Deformation Induced By Close-Proximity Bored Tunneling Using Distributed Optical Fiber Strain Measurements." *Proc. of ASCE* 307.84:1-13.

Naruse, H., K. Komatsu, K. Fujihashi and M. Okutsu. 2005. "Telecommunications tunnel monitoring system based on distributed optical fiber strain measurement." *Proc. of SPIE* 5855:168.

Nikles, M., L. Thevenaz, and P. Robert. 1997. "Brillouin Gain Spectrum Characterization in Single-mode Optical fibers." *Journal of Lightwave Technology* 15.10:1842-1851.

Zhang, C., W. Li, X. Bao, L. Chen, and M. Du. 2007. "Tensile Strain Dependence of the Brillouin Gain Spectrum in Carbon/polyimide Coated Fibers." *Optics Letters* 32.17:2565-2567.

Ou，J. P., Z. Zhou，and G. Chen. "Fiber Bragg Grating Sensors in Civil Engineering Applications." Chapter 8 in *Fiber Bragg Grating Sensors: Research Advancements, Industrial Applications and Market Exploration*, Edited by Dr. Andrea Cusano, Antonello Cutolo, and Jacques Albert from the Optoelectronic Division, Department of Engineering, University of Sannio, 82100 Benevento, Italy, Bentham Science Publishers, ISBN No. 978-1-60805-084-0, E-Book Program, www.bentham.org/ebooks, 2011.

Parker, T. R., M. Farhadiroushan, V. A. Handerek, and A. J. Rogers. 1997. "A Fully Distributed Simultaneous Strain and Temperature Sensor using Spontaneous Brillouin Backscatter." *IEEE Photonics Technology Letters* 9.7:979-981.

Rao, Y., J. D. C. Jones, H. Naruse, and R. I. Chen. 2002. "System for Measuring Temperature and Strain Separately by BOTDR and OTDR." *Proc. of SPIE* 4920:274.

Shi, B., H. B. Sui, J. Liu, D. Zhang, W. Zhang, and J. Q. Gao. 2005. "Study on BOTDR-based Distributed Optical Fiber Strain Measurement for Tunnel Health Diagnosis." *Chinese Journal of Rock Mechanics and Engineering* 24.15:2622-2628.

Shimada, A., H. Naruse, K. Uzawa, H. Murayama, and K. Kageyama. 2000. “Development of Integrated Damage Detection System for International America's Cup Class Yacht Structures Using a Fiber Optic Distributed Sensor.” *Proc. of SPIE* 3986:324.

Smith, J., A. Brown, M. D. Demerchant, and X. Bao. 1999. “Simultaneous Strain and Temperature Measurement Using a Brillouin-scattering-based Distributed Sensor.” *Proc. of SPIE* 3670:366.

Song, M. and X. Zhang. 2005. “Design and Realization of Brillouin Optical Time Domain Reflectometer with 34km in Sensing Length.” *Journal of Instrumentation* 26.11:1155-1158.

Tateda, M., T. Horiguchi. 1989. “Advances in Optical Time Domain Reflectometry.” *Journal of Lightwave Technology* 7.8:1217-1224.

Thevenaz, L., M. Nikles, A. Fellay, M. Facchini, and P. A. Robert. 1998. “Applications of Distributed Brillouin Fiber Sensing.” *Proc. of SPIE* 3407:374-381.

Wu, Z., B. Xu, K. Hayashi, and A. Machida. 2006. “Distributed Optic Fiber Sensing for a Full-scale PC Girder Strengthened with Prestressed PBO Sheets.” *Engineering Structures* 28: 1049-1059.

Yari, T., K. Nagai, and T. Shimuzi. 2003. “Overview of Damage Detection and Damage Suppression Demonstrator and Strain Distribution Measurement Using Distributed BOTDR Sensors.” *Proc. of SPIE* 5054:175.

Yu, Q., X. Bao, and L. Chen. 2004. “Simultaneous Strain and Temperature Measurement in PM Fibers Using Brillouin Frequency, Power and Bandwidth.” *Proc. of SPIE* 5391:301.

Xue, X. and Y. Gao. 2005. “Application of Distributed Optic Fiber Strain Measurement in Geological Hazards Prevention.” *The Chinese Journal of Geological Hazard and Control*., China.

Zhang, D., B. Shi., and H. Xu. 2004. “The BOTDR-based Strain Monitoring for Tunnel.” *Journal of Engineering Geology* 12:422-426.

Zhang, J., Y. E. Chuan, X. Xue, and Y. Gao. 2005. “The Application of BOTDR on Geological Hazards Monitoring in Three Gorges.” *Earth and Environment* 33.B10:355-358.

Zhou, Z., J. He, G. Chen, and J. Ou. 2009. “A Smart Steel Strand for the Evaluation of Prestress Loss Distribution in Post-tensioned Concrete Structures.” *Journal of Intelligent Material Systems and Structures* 20.16:1901-1912.

Zhou, Z., J. He, G. Chen, and J. Ou. 2009. “A New Kind of Smart Cable with Functionality of Full Scale Monitoring Using BOTDR Technique.” *Proc. of SPIE* 7293:72930L.

Zhou, Z., J. He, K. Yan, and J. Ou. 2008. “Fiber-reinforced Polymer-packaged Optical Fiber Sensors Based on Brillouin Optical-domain Analysis.” *Optical Engineering* 47.1:014401.

Zou, L., X. Bao, Y. Wan, F. Ravet, and L. Chen. 2004. “Centimeter Spatial Resolution of Distributed Optical Fiber Sensor for Structural Healthy Monitoring.” *Proc. of SPIE* 5579:1-10.